BioRxiv Submission, 6th April 2021

Eye morphogenesis in the blind Mexican cavefish

Lucie Devos[1], François Agnès[1], Joanne Edouard[2], Victor Simon[1,2], Laurent Legendre[2], Naima El Khallouki[2], Sosthène Barbachou[2], Frédéric Sohm[2] and Sylvie Rétaux[1*]

[1] Paris-Saclay Institute of Neuroscience, CNRS, Université Paris-Saclay, 91198 Gif sur Yvette, France,

[2] AMAGEN, CNRS, INRA, Université Paris-Saclay, 91198, Gif sur Yvette, France

* Correspondence: sylvie.retaux@cnrs.fr

Key words (6): *Zic1*; CRISPR/Cas9 knock-in; *Astyanax mexicanus*; live imaging, cell behaviors, optic vesicles

Abstract

The morphogenesis of the vertebrate eye consists of a complex choreography of cell movements, tightly coupled to axial regionalization and cell type specification processes. Disturbances in these events can lead to developmental defects and blindness. Here, we have deciphered the sequence of defective events leading to coloboma in the embryonic eye of the blind cavefish of the species *Astyanax mexicanus*. Using comparative live imaging on targeted enhancer-trap *Zic1:hsp70:GFP* reporter lines of both the normal, river-dwelling morph and the cave morph of the species, we identified defects in migratory cell behaviors during evagination which participate in the reduced optic vesicle size in cavefish, without proliferation defect. Further, impaired optic cup invagination shifts the relative position of the lens and contributes to coloboma in cavefish. Based on these results, we propose a developmental scenario to explain the cavefish phenotype and discuss developmental constraints to morphological evolution. The cavefish eye appears as an outstanding natural mutant model to study molecular and cellular processes involved in optic region morphogenesis.

Introduction

The morphogenesis of the vertebrate eye follows a complex choreography of cell movements, starting from a flat neural plate to generate a spherical multi-layered structure. This process is advantageously investigated on teleost models, which are amenable to live imaging (reviewed in (Cavodeassi, 2018).

At the end of gastrulation, the "eyefield" is specified in the anterior neural plate, surrounded anteriorly and laterally by the prospective telencephalon, and posteriorly by the future hypothalamus and diencephalon (Varga et al., 1999; Woo and Fraser, 1995; Woo et al., 1995). The first step of eye formation is the lateral evagination of the optic vesicles (OV) (England et al., 2006; Ivanovitch et al., 2013; Rembold et al., 2006). The vesicles then elongate due to a flow of cells entering the anterior/nasal OV, in a process recently re-described as "extended evagination" (Kwan et al., 2012). Simultaneously, the OVs are separated from the neural keel by the anterior-wards progression of a posterior furrow (England et al., 2006). Cells from the inner OV leaflet then migrate around the rim of the eye ventricle, the optic recess, into the lens facing neuroepithelium through the "rim movement" (Heermann et al., 2015; Kwan et al., 2012). The cells fated to the retinal pigmented epithelium (RPE) expand and flatten to cover the back of the retina (Cechmanek and McFarlane, 2017; Heermann et al., 2015). Together with the basal constriction of lens-facing epithelial cells (Martinez-Morales et al., 2009; Nicolas-Perez et al., 2016), these movements lead to optic cup (OC) invagination and also to the formation of the optic fissure - which needs to close to have a functional, round eye (Gestri et al., 2018). Finally, the entire eye, together with the forebrain, rotates anteriorly, bringing the fissure in its final ventral position. Hence, cells that are initially located in the dorsal or ventral part of the OV contribute to the nasal or temporal quadrant of the retina, respectively (Picker et al., 2009) (**Fig.S1**). Failure to complete correctly any of these steps can lead to vision defects; for example, failure to close properly the optic fissure is termed coloboma.

Astyanax mexicanus is a teleost that arises in two morphs: classical river-dwelling eyed morphs and blind cave-dwelling morphs. Although eyes are absent in adult cavefish, they first develop in embryos before degenerating during larval stages. The embryonic cavefish eyes

display several abnormalities: the OVs are short (Alunni et al., 2007), the OC and lens are small (Hinaux et al., 2015; Hinaux et al., 2016; Yamamoto and Jeffery, 2000) and the ventral OC is severely reduced or lacking, leaving the fissure wide open with a coloboma phenotype (Pottin et al., 2011; Yamamoto et al., 2004). Cavefish exhibit several modifications of morphogen expression which trigger changes of the cavefish eyefield and subsequent eye, and which have been linked to cavefish eye defects. Accordingly, overexpression of *Shh* in surface fish shortens its optic cups and triggers lens apoptosis, while inhibition of Fgf signalling in cavefish restores the ventral retina (Hinaux et al., 2016; Pottin et al., 2011; Torres-Paz et al., 2019; Yamamoto et al., 2004) .

Because of these variations, the cavefish is a remarkable natural mutant model to study eye development, beyond the mechanisms of eye degeneration and loss. Here, we sought better understanding cavefish embryonic eye defects as well as the mechanisms of eye morphogenesis in general. We generated CRISPR/Cas9-mediated targeted enhancer trap cavefish and surface fish *Zic1:hsp70:GFP* lines and performed comparative live imaging of eye morphogenesis in developing embryos of the two morphs to uncover the morphogenetic processes and cellular behaviors leading to cavefish coloboma.

Results and Discussion

Establishing *Zic1:hsp70:GFP* surface fish and cavefish knock-in reporter lines

We performed an *in situ* hybridization mini-screen to choose a candidate reporter gene labelling the entire optic region from neural plate stage (10hpf) until at least 30hpf (**Fig. S2A**). *Zic1* was chosen due to its early and persistent expression in the optic field (**Figure 1A**; **Fig. S2B** and legend), even though its pattern was complex and larger than the optic region.

We used a targeted enhancer-trap strategy into the *Zic1* locus, so that the GFP reporter insertion site would be similar in CF and SF lines and avoid positional effects, which is crucial for comparative purposes. The large and complex *Zic1* genomic region was examined to find conserved elements pointing toward putative regulatory elements (**Fig. 1BC**). In both zebrafish and *Astyanax* genomes (McGaugh et al., 2014), *Zic1* and *Zic4* were located in a head to head configuration in the middle of a gene desert (~275kb downstream of *Zic1* and ~235kb downstream of *Zic4* in *Astyanax)* which contained many fish-conserved elements, also partly conserved with tetrapods (**Fig. 1BC**). Such a regulatory landscape suggested that the elements driving *Zic1* expression are probably modular and difficult to identify, further strengthening the choice of a directed enhancer-trap approach. We thus "addressed" the enhancer-trap construct to *Zic1* downstream region using CRISPR/Cas9, similarly to the approach used by Kimura and colleagues (Kimura et al., 2014). We reasoned that using NHEJ (non-homologous end joining) DNA repair mechanism-based strategy, the preferred repair mechanism in fish embryos (Hagmann et al., 1998), would maximize integration efficiency. CF and SF eggs were co-injected with sgRNA2 (targeting the region between conserved non-coding elements 1 and 2), Cas9 protein and a linearized minimal promoter *hsp70:GFP* repair construct, and embryos were screened at 30hpf for fluorescence patterns consistent with *Zic1* endogenous expression (**Fig. 1E**). This method yielded good results, as its limited efficiency was compensated by the possibility of using a pattern-based fluorescence screening in F0 embryos. Excellent *Zic1* pattern recapitulation in F0 was observed at low frequency (1-2% of injected embryos), while other, more partial patterns were seen at higher frequencies. All potential founder embryos were raised until males were sexually mature (6 months) and could be screened by individual *in vitro* fertilization. We detected 3 founders for SF (out of 15 F0 males screened) and 5

113 founders for CF (out of 9 F0 males screened) with various transmission rates: 4%, 7% and 30%
114 for SF founders and 4%, 45%, 48%, 50% and 54% for CF founders, respectively. Hence, we
115 obtained an excellent ratio of founder fish among selected F0 embryos (>50% in cavefish). The
116 fish were screened based on their GFP pattern, matching *Zic1* (**Fig. 1E**). In both morphs some
117 variations in relative fluorescence intensities were observed, with some lines exhibiting
118 homogeneous expression levels and others showing strong GFP fluorescence in the
119 telencephalon and dimer fluorescence in the eye. We focused on the most homogeneous lines
120 for imaging purposes. Importantly, in those lines, genomic analyses confirmed the proper
121 insertion of the transgene at the targeted site, although some structural differences existed
122 (**Fig. S3**). The insertion method being based upon non-conservative NHEJ mechanism, these
123 variations are likely due to sequence differences from one line to another (indels or
124 duplications in genomic DNA or transgene), which may affect the nearby regulatory sequences
125 and slightly modify transgene expression. However, such variations remain anecdotal
126 compared to the differences observed between lines generated by traditional transgenesis
127 techniques (such as Tol2 transgenesis) (Elipot et al., 2014; Hinaux et al., 2015; Stahl et al.,
128 2019), validating this approach as a valuable tool to follow gene expression in *Astyanax*
129 morphotypes. Finally, double fluorescent *in situ* hybridisation for *Zic1* and *GFP* mRNAs
130 demonstrated that the reporter fully recapitulated the endogenous *Zic1* pattern at the stages
131 of interest (**Fig. 1F**).

132 CRISPR/Cas9 has been reported in surface *Astyanax mexicanus* to generate an *Oca2* null
133 mutant and to confirm the role of *Oca2* in the control of pigmentation (Klaassen et al., 2018).
134 This is to our knowledge the first report of the CRISPR/Cas9 technology used in this emergent
135 model species to generate identical reporter lines in the two morphotypes, and in a targeted
136 genome edition perspective.

137

138 **Comparing eye morphogenesis in surface fish and cavefish through live imaging**

139 Live imaging was performed on a light-sheet microscope on *Zic1:hsp70:GFP* lines from
140 ~10.5hpf to 24-30hpf (**Fig. 2** and **Movies 1 and 2**). Embryos were injected with H2B-mCherry
141 mRNA to follow cell nuclei. The orthogonal illumination of the SPIM induced minimal photo-
142 damage, and embryos developing for more than 20hours under the microscope were alive

143 with a normal head shape at 48-60hpf -even though the tail was usually twisted due to the
144 mechanical constraint in the low-melting agarose.

145 For analysis, we chose a plane crossing the middle of the lens and the optic stalk (lines on **Fig.**
146 **2A**), to follow the anterior rotation of the eye. Overall, optic morphogenesis in SF
147 recapitulated the events described in zebrafish, while in CF the movements were conserved
148 but their relative timing and extent appeared different. The following macroscopic analyses
149 result from quantifications made on n=4 eyes for each morph.

150

151 ***Evagination and elongation of the OVs*.** The CF OVs were about half-shorter than the SF OVs
152 from the beginning of evagination onwards (139µm *vs* 216µm at 11.5hpf) (**Fig. 2A-C**).
153 Elongation progressed at about the same pace as in SF until 17.5hpf (**Fig. 2C**). However, while
154 OV length decreased between 17.5-25.5hpf in SF due invagination, elongation continued at
155 slower pace until 25.5hpf in CF (**Fig. 2CD**). Moreover, the final size of the SF OC was very similar
156 to the early evaginating eyefield (240µm at 10.5hpf *vs* 252µm at 31.5hpf) while in CF a net
157 increase was observed (146µm at 10.5hpf *vs* 186µm at 31.5hpf) (**Fig. 2C**). In addition, in SF the
158 OVs remained closely apposed to the neural tube, while in CF they first started growing away
159 before getting back closer between 18.5-21.5hpf (**Fig. 2B**). Finally, throughout development,
160 the width of the optic stalk (defined in its wide meaning as the connection between OVs and
161 neural tube) was similar in the two morphs (**Fig. S4**), despite an initially smaller size in CF due
162 to the smaller OVs.

163 Since elongation proceeds at a similar rate in CF and SF until 17.5hpf, the shorter size of the
164 cavefish OV (Alunni et al., 2007; Strickler et al., 2001) seems principally due to the small size
165 of the initial eyefield (Agnès et al., 2021). Of note, albeit smaller, CF OVs seem "correctly"
166 patterned in their future naso-temporal axis, according to *FoxG1* and *FoxD1* markers at
167 13.5hpf (Hernandez-Bejarano et al., 2015). Then, after the initial evagination and patterning
168 of small OVs, morphogenesis proceeds with the extended evagination, whereby cells from the
169 neural tube continue entering the OV to contribute exclusively to the ventro-nasal part of the
170 eye (Kwan et al., 2012). Our measurements suggest that this step proceeds normally in CF.
171 This could partially compensate the originally small size of the eyefield/OV, but only in the
172 nasal part, while the temporal part would remain affected in size.

173

174 ***Optic cup invagination and lens formation*.** The posterior end of the OVs started curling back
175 in both CF and SF around 15.5hpf. The lens was identifiable as an ectodermal thickening at
176 17.5hpf (**Fig. 2B** and **movies 1 and 2**), in a central position with regard to the antero-posterior
177 extension of the OV, in both morphs (**Fig. 2B**,**F**). Then, in SF, invagination quickly brought closer
178 the two OC edges in contact with the lens (**Fig. 2B**,**E**). In contrast, despite initially harbouring
179 a curvature typical of invagination, in CF the OC edges remained flat, with an apparent
180 impairment of the rim movement in their posterior part (**Fig. 2B**,**E and Movie 2**). The CF OVs
181 continued to elongate while the lens remained static, therefore shifting the lens position
182 anteriorly (**Fig. 2B,F**). The posterior OC showed slow and reduced curling, which in some cases
183 led to a separation from the lens. Eventually, the posterior (prospective dorsal) OC finally
184 curved and contacted the lens (**Movie 2**; **Fig. 2B**), but remained shallower with small bulging
185 lens.

186 Thus, although the invagination in CF seems to start normally between 15.5-19.5hpf, it
187 progresses poorly so that the OCs remain elongated. This timing is reminiscent of the two
188 steps described for OC invagination in zebrafish: basal constriction initiates the primary folding
189 between 18-20hpf (18-22ss), followed by the rim movement which brings the presumptive
190 retina from the inner OV leaflet into the lens-facing epithelium by an active migration around
191 the rims of the optic recess between 20-24hpf (Heermann et al., 2015; Nicolas-Perez et al.,
192 2016; Sidhaye and Norden, 2017). In *Astyanax*, 18ss corresponds to ~16.5hpf (Hinaux et al.,
193 2011), suggesting that the initial basal constriction leading to the onset of OC invagination is
194 conserved in cavefish. In contrast, the prolonged extension and the weak curvature of the OVs
195 suggest that the rim movement must be impaired. We suggest that a continuous flow of cells
196 entering the retina leads to its elongation, in the absence of an efficient rim movement. The
197 later is weaker but not absent in CF, as the posterior OC still manages to contact the lens, but
198 at later stages. Such defective rim movement might be due to various causes, such as defects
199 in the basal membrane or failure to establish proper focal adhesion as seen in the *ojoplano*
200 medaka mutant (Martinez-Morales et al., 2009; Nicolas-Perez et al., 2016; Sidhaye and
201 Norden, 2017). Alternatively, active migration could be altered by extrinsic signals, as in BMP
202 overexpression experiments where the cell flow toward the lens-facing epithelium is reduced
203 (Heermann et al., 2015). The various morphogen modifications known in cavefish, and the fact

204 that the ventral eye can be restored by delaying the onset of Fgf signalling in CF to match the
205 SF timing (Pottin et al., 2011), support this possibility.

206 It was proposed that spreading and migration of RPE cells is concomitant with the rim
207 movement and may contribute to it as a driving force (Cechmanek and McFarlane, 2017;
208 Moreno-Marmol et al., 2018). In 36hpf SF embryos, the RPE marker *Bhlhe40* was expressed
209 all around the eye, often contacting the lens (**Fig. 2GH**), which we took as an indicator of the
210 correct engulfment of the retina by the migrating RPE. The expression spanned 326° around
211 the eye (**Fig. 2GH**). Conversely, in CF, *Bhlhe40* expression showed a significantly diminished
212 covering of the retina by the RPE (289°), with a wider ventral gap possibly corresponding to
213 wider optic fissure opening and *Bhlhe40*-positive cells further away from the lens, suggesting
214 reduced or delayed retina covering by the RPE (**Fig. 2GHI**). At 48hpf however, the staining span
215 was no longer different from the 36hpf SF. These data show that RPE identity is maintained in
216 the CF eye, yet the expansion and engulfment movement of this tissue to cover the whole
217 retina is delayed compared to SF - reinforcing the idea that the rim movement is impaired in
218 cavefish. Potentially, RPE spreading may also be involved in optic fissure closure, as suggested
219 by the presence of a coloboma upon impairment of the rim movement by *BMP4*
220 overexpression in the OV (Heermann *et al.*, 2015). Deficiency in RPE spreading might
221 participate in the cavefish coloboma phenotype (**Fig. 2I**). Interestingly, the transplantation of
222 a healthy SF lens into the CF OC rescues the eye as a structure, i.e., prevents lens-induced
223 degeneration, but does not rescue coloboma (Yamamoto and Jeffery, 2000). This is consistent
224 with our findings showing that improper closure of the fissure is autonomous to CF retinal
225 tissues and results from defective morphogenetic movements.

226 Finally, our movies show that the lens forms in proper place and time, in both morphs, with
227 regard to initial OC invagination. It is only at later stages that the lens appears more anterior
228 (i.e., facing the presumptive ventral retina after final eye rotation) in cavefish. This apparent
229 displacement of the lens relative to the retina is not due to a movement of the lens itself -
230 which remains fixed throughout eye morphogenesis (Greiling and Clark, 2009), attached to
231 the overlying ectoderm from which it delaminates around 22hpf in *Astyanax* (Hinaux et al.,
232 2017) -but rather to persistent OV elongation. This suggests that proper initial interactions
233 occur between the central OV and the lens to adjust their relative position and to initiate OC
234 invagination. Indeed, in chick, the pre-lens ectoderm is required for OC invagination while the

235 lens placode itself is dispensable (Hyer et al., 2003). In cavefish, such mechanisms could exist
236 and lead to the proper initiation of OC folding, as we have observed. Finally, the anterior-
237 shifted position of the lens, due to elongation without invagination, explains how the lens is
238 ventrally-displaced in the mature CF eye after the final anterior rotation movement, leading
239 to coloboma (**Fig. 2A and I**).

240

241 In sum, our live-imaging experiments suggest that, in CF (1) OVs are reduced in size after the
242 initial evagination, (2) OV elongation occurs properly, while (3) invagination is transiently
243 compromised. Below we started addressing the cellular behaviors that may underlie these
244 phenotypes.

245

246 **Comparing cell behaviors in surface fish and cavefish during evagination**

247 To study cell behaviors that might contribute to the small size of CF OVs, we tracked cells
248 during evagination, between 11.5hpf-13hpf (1h40, 40 movie frames).

249

250 ***OV cells proliferation.*** Division rates may account for size differences between SF and CF OVs.
251 To test this hypothesis, we reconstructed the complete mitotic pattern of the anterior neural
252 tube or head, in one CF and one SF embryo. Metaphase plates were searched manually and
253 tracked at each time step through the depth of the embryos (**Movies 3-6 and Fig. 3AB**). A total
254 of 1073 and 803 cell divisions were annotated in SF and CF, respectively, during the 100min
255 studied. It is, to our knowledge, the first report providing an estimation of the mitotic rate,
256 ~10 mitoses per minute in the brain/head, during fish neurulation, and a description of cell
257 mitotic behaviors in the evaginating OVs. In both morphs, mitoses were evenly distributed in
258 time and in space - not considering the strong tendency of mitoses to occur close to ventricles
259 (below and **Fig. S5**). After manual re-segmentation through movie stacks to count mitoses in
260 regions of interest, we found about twice more cell divisions in the SF than in the CF OVs
261 (mean left/right: 154/SF *vs* 67/CF) (**Fig. 3A-E; Fig. S6**). The same was true for the "prospective
262 lens", i.e. the ectoderm in direct contact with the OVs (17/SF *vs* 7/CF). Such SF/CF difference
263 in the number of mitoses was not observed in a medial neural tube region used as control

264 (157/152)(**Fig. 3DE**). In both OVs and presumptive lens ectoderm, the left/right symmetry of
265 mitoses distributions and numbers was excellent, suggesting that the mitotic landscape was
266 accurately reconstituted. To compare mitotic rates in SF and CF optic tissues, the numbers of
267 mitoses were normalized to OV volumes, in two different ways (**Fig. 3CDE; Fig. S6**).
268 Unexpectedly, the normalized mitotic activity appeared higher in cavefish OVs, suggesting
269 that proliferative activity in the CF optic region somehow tends to compensate for small
270 eyefield size (Agnès et al., 2021), and in any case does not participate in the establishment of
271 OV size differences. Importantly, the mitotic behaviors of SF and CF optic cells were also
272 qualitatively identical. The migration towards the ventricle (optic recess), the
273 orienting/rotating behavior of metaphasic plate cells before dividing, and the post-mitosis
274 integration of daughter cells into the neuroepithelium were systematically observed in both
275 morphs (**Fig. 3F-I**; **Fig. S7**). These results rule out an early proliferative defect in CF OVs to
276 explain their small size, which parallels studies at later stages which dismissed a role for
277 defective proliferation during CF eye degeneration (Alunni et al., 2007; Strickler et al., 2002).
278 The cavefish OVs also appear like an outstanding model to study developmental mechanisms
279 controlling organ size and developmental robustness (Young et al., 2019).

280

281 ***OV cells trajectories.*** Defective migratory properties might also contribute to the formation
282 of small OVs in CF. To test this hypothesis, 24 SF and 44 CF OV cells were tracked between
283 11.5hpf-13hpf (**Fig. 4**).

284 In SF, we observed markedly different types of trajectories depending on the initial position
285 of cells. Namely, cells located in the 2/3 anterior OV showed a lateral-wards movement with
286 a slight tendency to dive towards the ventral side, thus strongly contributing to evagination
287 (**Fig. 4A-B**). Some anterior cells, either dorsally or ventrally located, also made a posterior turn
288 or had a strict antero-posterior trajectory, potentially contributing to elongation (**Fig. 4A-B**).
289 Conversely, cells located in the posterior third of OVs followed a dorsal-wards and inwards
290 path, seemingly imposing a rotational movement to the posterior OV (**Fig. 4A-B**), and
291 putatively corresponding to the “pinwheel movement” described in zebrafish by (Kwan et al.,
292 2012).

293 Most of these trajectories were impaired in CF (**Fig. 4A-B**). Anterior cells showed reduced
294 outwards movement and remained static in Z, showing reduced contribution to evagination.
295 Posterior cells trajectories had less amplitude in the upwards direction and displayed
296 outwards instead of inwards trajectories. On the other hand, cells with posterior-wards
297 trajectories contributing to elongation were observed in CF (**Fig. 4A**), in line with the proper
298 elongation recorded above (**Fig. 3**). These data suggested that CF optic cells adopted improper
299 behaviors in terms of trajectories during evagination.

300 We analysed kinetic parameters of cell migrations. The instantaneous speed and the total
301 distance travelled by OV cells in the two morphs were similar (**Fig. 4C**), suggesting that the
302 migrating apparatuses and capacities of CF cells were unaffected. However, the total
303 displacement in space was markedly shorter for CF cells, in line with above observations on
304 trajectories. To reconcile these apparently contradictory observations, we measured
305 deviation angles of cell trajectories between different time steps. We found a significant
306 zigzagging or erroneous aspect of CF cells migration, as compared to the straighter paths of
307 SF cells (**Fig. 4C**). These data suggest that CF optic cells partly lacked or failed to respond to
308 guidance and directionality cues.

309

310 **Conclusions**

311 In all eyeless or eye-reduced cave vertebrates examined so far, initial eye development occurs
312 (e.g., (Durand, 1976; Stemmer et al., 2015; Wilkens, 2001). This represents an energetically-
313 costly process for embryos, raising the puzzling question of why would these species first
314 develop eyes which are after all fated to degeneration, and suggesting that initial eye
315 development cannot be circumvented (Rétaux and Casane, 2013). Our results help refine the
316 step(s) in eye morphogenesis that are subjected to developmental constraint. In cavefish, the
317 eyefield is specified and the evagination/elongation steps, corresponding to cell movements
318 leading to the sorting of retinal versus adjacent telencephalic, preoptic and hypothalamic cells
319 of the neural tube, do occur. It is only after the segregation between these differently-fated
320 cell populations that cavefish eye morphogenesis starts going awry, with a defective
321 invagination process, soon followed by lens apoptosis and progressive degeneration of the
322 entire eye. Therefore, our data support the idea that the first steps of eye development

323 constitute an absolute developmental constraint to morphological evolution. To the best of
324 our knowledge, the closest to a counter-example is the medaka mutant *eyeless*, a
325 temperature-sensitive *rx3* mutant line in which OVs do not evaginate. However, the
326 homozygous *eyeless* fish either die after hatching (Winkler et al., 2000) or, for the 1% which
327 reach adulthood, are sterile probably due to anatomical hypothalamic or hypophysis defects

328 (Ishikawa et al., 2001) -still reinforcing the hypothesis of a strong developmental constraint
329 on vertebrate eye morphogenesis.

330 Thanks to genome-editing and live-imaging methods, we have started deciphering the
331 morphogenetic and cellular processes underlying colobomatous eye development in cavefish.
332 Further analyses will refine the current scenario. Our data also pave the way for experiments
333 aiming at understanding the defective molecular or signalling mechanisms in cavefish eye
334 morphogenesis, using the *Zic1:hsp70:GFP* knock-in lines and embryology methods we have
335 recently developed (Torres-Paz and Rétaux, 2021).

336

337

338

339

Methods

Animals

Laboratory stocks of *A. mexicanus* surface fish and cavefish were obtained in 2004 from the Jeffery laboratory at the University of Maryland. The surface fish were originally collected from San Solomon Spring, Texas and the cavefish are from the Pachón cave in Mexico. Surface fish are kept at 26°C and cavefish at 22°C. Natural spawns are induced after a cold shock (22°C over weekend) and a return to normal temperature for surface fish; cavefish spawns are induced by raising the temperature to 26°C. Embryos destined for *in situ* hybridization were collected after natural spawning, grown at 24°C and staged according to the developmental staging table (Hinaux et al. 2011) and fixed in 4% paraformaldehyde. After progressive dehydration in methanol, they were stored at -20°C. Embryos destined to transgenesis or live imaging were obtained by *in vitro* fertilization. Embryos were raised in an incubator until 1 month post fertilization for the surface fishes and two month post fertilization for the cavefish. They were kept at low density (15/20 per litre maximum) in embryo medium, in 1 litre plastic tanks with a soft bubbling behind the strainer. Larvae were fed from day 5 with paramecium and transitioned to artemia nauplii from day 10-15. Artemia were given twice a day except for the weekends (once a day) and carefully removed afterward to avoid polluting the medium. At least two thirds of the medium were changed every day and dead larvae removed. After one month for the surface fish and two months for the cavefish, juveniles were taken to the fish facility where they were fed dry pellets (Skretting Gemma wean 0.3) and quickly moved to bigger tanks in order to allow their fast growth.

Animals were treated according to French and European regulations of animals in research. SR' authorization for use of animals in research is 91-116, and Paris Centre-Sud Ethic committee authorization numbers are 2012-52 and 2012-56.

In situ hybridization

Some cDNAs were available from our cDNA library : *Zic1* (FO290256), *Zic2a* (FO320762) and *Rx3* (FO289986); others were already cloned in the lab : *Lhx2* (EF175737) and *Lhx9* (EF175738)

369 (Alunni et al. 2007); obtained from other labs (*Vax1* : Jeffery lab, University of Maryland;
370 (Yamamoto et al. 2004)); or cloned for the purpose of this work in pGEMT-Easy (Promega) :

371 - Vax2: forward primer GGGCAAAACATGCGCGTTA; reverse primer
372 CAGTAATCCGGGTCCACTCC.
373 - Bhlhe40: forward primer : GCACTTTCCCTGCGGATTTC; reverse primer :
374 TGGAGTCTCGTTTGTCCAGC

375 cDNAs were amplified by PCR, and digoxygenin-labelled riboprobes were synthesized from
376 PCR templates. Embryos were rehydrated by graded series of EtOH/PBS, then for embryos
377 older than 24hpf, proteinase-K permeabilization at 37°C was performed for 36hpf embryos
378 only (10 µg/ml, 15 min) followed by a post-fixation step. Riboprobes were hybridized for 16
379 hr at 65°C and embryos were incubated with anti-DIG-AP (Roche, dilution 1/4000) overnight
380 at 4°C. Colorimetric detection with BCIP/NBT (Roche) was used. Mounted embryos were
381 imaged on a Nikon Eclipse E800 microscope equipped with a Nikon DXM 1200 camera running
382 under Nikon ACT-1 software. Brightness and contrast were adjusted using FIJI, some of the
383 images used for illustration purpose were created from an image stack, using the extended
384 depth of field function of Photoshop CS5. Area, distance and angle measurements were
385 performed using FIJI (Schindelin et al., 2012).

386

387 **In vitro fertilization (IVF) and injections**

388 Surface and cavefish were maintained in a room with shifted photoperiod (light: 4pm – 7am,
389 L:D 15:11) in order to obtain spawns during the working day (*Astyanax* spawn at night (Simon
390 et al., 2019)). Fish activity was monitored after induction and upon visible excitation or when
391 first eggs were found at the bottom of the tank, fish were fished. Females were processed first
392 to obtain eggs: they were quickly blotted on a moist paper towel and laid on their side in a
393 petri dish. They were gently but firmly maintained there while their flank was gently stroked.
394 If eggs were not released immediately, the female was put back in the tank. Once eggs were
395 collected, a male was quickly processed similarly to females, on the lid of the petri dish to
396 collect sperm. The sperm was then washed on the eggs with 10-20mL of tank water
397 (conductivity ~500µS) and left for a few moments (30s to 2 min approximatively), after which
398 embryo medium was added in the petri dish. Fertilised eggs were quickly laid on a zebrafish

399 injection dish containing agarose grooves. They were injected with a Picospritzer III (Parker
400 Hannifin) pressure injector.

401

402 **CRISPR injections and Knock-In lines**

403 sgRNA were designed to target the low-conservation regions between elements 1 and 2 and
404 between elements 3 and 4. Two sgRNA were initially designed per region and sgRNA2 was
405 found to efficiently cut the targeted region (**Fig. S8)**. The mix contained Cas9 protein
406 generously provided by TACGENE and sgRNA2 with the following targeting sequence:
407 CCCAATTCACCAGTATACGT (synthesized with AMBION T7 MEGAshortscript™ T7 transcription
408 kit). Concentrations were kept with a 1:1.5 Cas9 to sgRNA molar ratio and varied between
409 0.71µM (25ng/µL) and 5.67µM (200ng/µL) of sgRNA 2, mostly 2.84 and 1.42µM were used.
410 The donor construct contained a HSP70 promoter used as a minimal promoter, a GFP cDNA
411 and SV40 poly-adenylation signal, flanked by I-SceI meganuclease cutting sites. I-SceI was used
412 to generate sticky ends and was either detached by 7 min at 96°C or injected with the
413 construct. Concentrations of the repair construct varied between 3.33 and 10.92nM but were
414 mostly used at 10.71nM.

415

416 **mRNA injection**

417 Transgenic embryos used for live imaging were injected in the cell or yolk at 1 cell stage with
418 a H2B-mCherry fusion mRNA at a concentration of 50ng/µL.

419

420 **Imaging**

421 Transgenic embryos were obtained by IVF with wild-type eggs and transgenic sperm and were
422 immediately injected with H2B-mCherry mRNA for nuclear labelling. Injected embryos were
423 screened for GFP and mCherry fluorescence under a Leica M165C stereomicroscope around
424 10-11hpf, when GFP reporter fluorescence first becomes detectable.

425 Selected embryos were immediately mounted in a phytagel tube (SIGMA, CAS Number:
426 71010-52-1) molded with Phaseview Teflon mold (1.5mm of diameter) and maintained in

427 position with 0.4% low melting point agarose (Invitrogen UltraPure™ Low Melting Point
428 Agarose). The tube containing the embryo was placed horizontally into the chamber
429 containing 0.04% Tricaine in embryo medium (Sigma, CAS Number: 886-86-2). The tube was
430 rotated under the microscope so that the embryo would face the objective.

431 Live imaging was performed approximately from 10.5-11hpf to 24hpf every 2.5min-3min,
432 using a Phaseview Alpha^3 light sheet apparatus, coupled with an Olympus BX43 microscope
433 and using either a 20X/NA 0.5 Leica HCX APO objective or a 20X/NA 0.5 Olympus objective.
434 Images were acquired using QtSPIM software (Phaseview), which controlled a Hamamatsu
435 ORCA-Flash4.0 Digital sCMOS camera.

436 Room temperature was maintained at 24°C by air conditioning and the chamber temperature
437 was further controlled by a BIOEMERGENCES-made thermostat. Medium level was
438 maintained by a home-made perfusion system and an overflow to renew the medium.

439

440 **Movie analyses**

441 Morphogenesis

442 Images were obtained and visualized with Arivis Vision4D software using re-oriented 3D stacks
443 to allow similar optical section plane of analysis in different samples, cutting through the
444 middle of the lens and the optic stalk at all time-steps. On one time-step per hour,
445 measurements were performed on the re-oriented images: optic vesicle/optic cup length (at
446 the widest), OV size increase (calculated by subtracting the length at the onset of furrow
447 formation to the length at time t), optic stalk width, distance between the anterior optic cup
448 and the lens, distance between the posterior optic cup and the lens, distance between the
449 optic cup edges, position of the lens relative to anterior OV (=distance between center of the
450 lens and anterior OV / (distance between center of the lens and anterior OV + distance
451 between center of the lens and posterior OV) (see schemes on **Fig. 2** and **Fig. S4**).

452 Image stack treatments for cell tracking

453 Hyper-stacks used for tracking analyses were in 8-bit format. Pixel dimensions were 0.3 µm in
454 x y, 1 µm in z, 39 t frames (2min30 each) and 420 and 360 z steps, respectively for surface fish
455 and cavefish embryo. To improve image quality and allow more convenient tracking in

456 MAMUT, several image treatments were necessary. Pixel intensity of all images within each
457 stack were homogenized using contrast enhancement (0.3%), and 3D drift correction to
458 improve image alignment was performed. Image stack were registered in the H5 format.

459 Cell tracking

460 To study cell behaviors, we tracked cell nuclei during evagination, between 11.5hpf and 13hpf
461 (1h40, 40 movie frames) using the Fiji plugin MAMUT (Schindelin et al., 2012; Wolff et al.,
462 2018) which allowed identification of nuclei at each t frame in the 3D. Because of the 3-fold
463 increased voxel size compared to x and y, nuclei appeared distorted in the z plane. We
464 preferentially –but not exclusively- tracked nuclei of high fluorescence intensity, which greatly
465 facilitated non-ambiguous nuclei tracking. All nuclei tracks used for trajectory analyses were
466 meticulously analysed and checked twice.

467 For trajectory analyses, the (x,y,z) cell coordinates were extracted using MAMUT and
468 distances in 3D or 2D (x,y) between time points were calculated using the Pythagoras formula.
469 We used x,y,z coordinates to calculate cumulative distance and absolute distance in space
470 covered in 3D as well as instantaneous migration speeds (distance covered/150 sec). For the
471 trajectory aspect, we used x,y coordinates to calculate instantaneous deviation angle at each
472 time point using the Al-Kashi formula, valid in any triangle ABC, which relates the length of the
473 sides using the cosine of one of the angles of the triangle. We calculated the value of the angle
474 AB^AC in a triangle ABC, in which AB, BC and AC sides represent the distances covered by a
475 nucleus between (t-t+1), (t+1-t+2) and (t-t+2), respectively. AB^AC=DEGRES(ACOS(((BC^2)-
476 (AB^2)-(AC^2))/-(ACxBC/2))).

477 To study proliferative activity, we tracked metaphases and anaphases manually and
478 exhaustively in the whole brain /head of one SF and one CF embryo. To count mitotic events
479 in OVs and presumptive lens without errors, each mitosis tracked and labelled in MAMUT was
480 re-checked and allocated manually to structures or regions of interest (roi) (see **Fig. S6**).
481 Results were expressed either as absolute cell counts, or normalized and expressed as
482 densities to account for the difference of OV size between SF and CF (see **Fig. S6**). Two types
483 of normalizations were applied, which lead to the same conclusion. First, the mitoses counts
484 were normalized to the OV volumes, calculated on the movies using the plugin MZstack at
485 11.5, 12.5 and 13.5hpf and averaged (**Fig.3E**). Second, the mitoses counts were performed on

486 maximum projections inside rois (regions of interest) of identical size, in the OVs or in the
487 medial neural tube as a control (see **Fig. S6**). In the case of the OV roi, and because the optic
488 vesicles are smaller in x,y but also in z (depth) in CF, a normalisation factor was applied. In SF,
489 OV cell divisions were tracked along a z extent of 145, while in CF cell divisions were tracked
490 on a z extent of 100. The normalisation factor was therefore x1.45 (**Fig. 3E**). For this
491 proliferation analysis, statistical comparison could not be provided as we studied one SF and
492 one CF sample.

493

494 **Statistics**

495 Statistical significance and p-values were calculated using non-parametric Mann-Whitney U
496 tests in R. No statistical method was used to predetermine sample size. The experiments were
497 not randomized and the investigators were not blinded during image analyses.

Acknowledgements

Work supported by an Equipe FRM grant (DEQ20150331745), UNADEV/AVIESAN and Retina France grants to SR. We thank Jean-Paul Concordet and Anne De Cian (Tacgene, Sorbonne Universités, Paris) for sharing Cas9 protein; Diane Denis, Krystel Saroul, Jocelyne Gaget, the Amagen personnel for advices and care of our *Astyanax* colony; Patrick Para for making custom tools for live microscopy; Adeline Boyreau, Adeline Rausch, Fanny Husson, Elena Kardash and Nadine Peyrieras (BioEmergence, Gif sur Yvette, France) for reagents, discussions and advices on live imaging, and for the use of the SPIM and image analysis tools; Cyprian Wozniak, Arthur Le Bris and Gaël Launay from PhaseView (Verrière-le-Buisson, France) for technical support and development of tools on the light-sheet microscope; Guillaume Plongeon for volume analyses; Martin Pepin (Sorbonne Université) for writing an essential macro in FIJI and Romain Le Bars at the I2BC Imaging Plateform facility for assistance on the FIJI software; Jean Yves Tinevez and the Image Analysis Hub at the Institut Pasteur (Paris) for help with tracking strategy.

References

Agnès, F., Torres-Paz, J. and Rétaux, S. (2021). A comparative 3D map of the neural plate challenges current view of vertebrate eyefield specification. *BioRxiv, preprint*.

Alunni, A., Menuet, A., Candal, E., Penigault, J. B., Jeffery, W. R. and Rétaux, S. (2007). Developmental mechanisms for retinal degeneration in the blind cavefish Astyanax mexicanus. *J Comp Neurol* **505**, 221-33.

Cavodeassi, F. (2018). Dynamic Tissue Rearrangements during Vertebrate Eye Morphogenesis: Insights from Fish Models. *J Dev Biol* **6**.

Cechmanek, P. B. and McFarlane, S. (2017). Retinal pigment epithelium expansion around the neural retina occurs in two separate phases with distinct mechanisms. *Dev Dyn* **246**, 598-609.

Deschet, K., Bourrat, F., Ristoratore, F., Chourrout, D. and Joly, J. S. (1999). Expression of the medaka (Oryzias latipes) Ol-Rx3 paired-like gene in two diencephalic derivatives, the eye and the hypothalamus. *Mech Dev* **83**, 179-82.

Durand, J. P. (1976). Ocular development and involution in the European cave salamander, Proteus anguinus laurenti. *Biol Bull* **151**, 450-66.

Elipot, Y., Legendre, L., Père, S., Sohm, F. and Rétaux, S. (2014). Astyanax transgenesis and husbandry: how cavefish enters the lab. *Zebrafish* **11 (4)**, 291-299.

England, S. J., Blanchard, G. B., Mahadevan, L. and Adams, R. J. (2006). A dynamic fate map of the forebrain shows how vertebrate eyes form and explains two causes of cyclopia. *Development* **133**, 4613-7.

Gestri, G., Bazin-Lopez, N., Scholes, C. and Wilson, S. W. (2018). Cell Behaviors during Closure of the Choroid Fissure in the Developing Eye. *Front Cell Neurosci* **12**, 42.

Greiling, T. M. and Clark, J. I. (2009). Early lens development in the zebrafish: a three-dimensional time-lapse analysis. *Dev Dyn* **238**, 2254-65.

Hagmann, M., Bruggmann, R., Xue, L., Georgiev, O., Schaffner, W., Rungger, D., Spaniol, P. and Gerster, T. (1998). Homologous recombination and DNA-end joining reactions in zygotes and early embryos of zebrafish (Danio rerio) and Drosophila melanogaster. *Biol Chem* **379**, 673-81.

Heermann, S., Schutz, L., Lemke, S., Krieglstein, K. and Wittbrodt, J. (2015). Eye morphogenesis driven by epithelial flow into the optic cup facilitated by modulation of bone morphogenetic protein. *Elife* **4**.

Hernandez-Bejarano, M., Gestri, G., Spawls, L., Nieto-Lopez, F., Picker, A., Tada, M., Brand, M., Bovolenta, P., Wilson, S. W. and Cavodeassi, F. (2015). Opposing Shh and Fgf signals initiate nasotemporal patterning of the zebrafish retina. *Development* **142**, 3933-42.

Hinaux, H., Blin, M., Fumey, J., Legendre, L., Heuze, A., Casane, D. and Rétaux, S. (2015). Lens defects in Astyanax mexicanus Cavefish: Evolution of crystallins and a role for alphaA-crystallin. *Dev Neurobiol*, 505-21.

Hinaux, H., Devos, L., Bibliowicz, J., Elipot, Y., Alié, A., Blin, M. and Rétaux, S. (2016). Sensory evolution in blind cavefish is driven by early events during gastrulation and neurulation. *Development* **143**, 4521-4532.

Hinaux, H., Pottin, K., Chalhoub, H., Pere, S., Elipot, Y., Legendre, L. and Rétaux, S. (2011). A developmental staging table for Astyanax mexicanus surface fish and Pachon cavefish. *Zebrafish* **8**, 155-65.

Hinaux, H., Recher, G., Alie, A., Legendre, L., Blin, M. and Retaux, S. (2017). Lens apoptosis in the Astyanax blind cavefish is not triggered by its small size or defects in morphogenesis. *PLoS One* **12**, e0172302.

Hyer, J., Kuhlman, J., Afif, E. and Mikawa, T. (2003). Optic cup morphogenesis requires pre-lens ectoderm but not lens differentiation. *Dev Biol* **259**, 351-63.

Ishikawa, Y., Yoshimoto, M., Yamamoto, N., Ito, H., Yasuda, T., Tokunaga, F., Iigo, M., Wakamatsu, Y. and Ozato, K. (2001). Brain structures of a medaka mutant, el (eyeless), in which eye vesicles do not evaginate. *Brain Behav Evol* **58**, 173-84.

Ivanovitch, K., Cavodeassi, F. and Wilson, S. W. (2013). Precocious acquisition of neuroepithelial character in the eye field underlies the onset of eye morphogenesis. *Dev Cell* **27**, 293-305.

Kimura, Y., Hisano, Y., Kawahara, A. and Higashijima, S. (2014). Efficient generation of knock-in transgenic zebrafish carrying reporter/driver genes by CRISPR/Cas9-mediated genome engineering. *Sci Rep* **4**, 6545.

Klaassen, H., Wang, Y., Adamski, K., Rohner, N. and Kowalko, J. E. (2018). CRISPR mutagenesis confirms the role of oca2 in melanin pigmentation in Astyanax mexicanus. *Dev Biol* **441**, 313-318.

Kwan, K. M., Otsuna, H., Kidokoro, H., Carney, K. R., Saijoh, Y. and Chien, C. B. (2012). A complex choreography of cell movements shapes the vertebrate eye. *Development* **139**, 359-72.

Martinez-Morales, J. R., Rembold, M., Greger, K., Simpson, J. C., Brown, K. E., Quiring, R., Pepperkok, R., Martin-Bermudo, M. D., Himmelbauer, H. and Wittbrodt, J. (2009). ojoplano-mediated basal constriction is essential for optic cup morphogenesis. *Development* **136**, 2165-75.

566 **Maurus, D. and Harris, W. A.** (2009). Zic-associated holoprosencephaly: zebrafish Zic1 controls midline formation
567 and forebrain patterning by regulating Nodal, Hedgehog, and retinoic acid signaling. *Genes Dev* **23**, 1461-73.
568 **McGaugh, S. E., Gross, J. B., Aken, B., Blin, M., Borowsky, R., Chalopin, D., Hinaux, H., Jeffery, W. R., Keene, A.,**
569 **Ma, L. et al.** (2014). The cavefish genome reveals candidate genes for eye loss. *Nat Commun* **5**, 5307.
570 **Moreno-Marmol, T., Cavodeassi, F. and Bovolenta, P.** (2018). Setting Eyes on the Retinal Pigment Epithelium.
571 *Front Cell Dev Biol* **6**, 145.
572 **Nicolas-Perez, M., Kuchling, F., Letelier, J., Polvillo, R., Wittbrodt, J. and Martinez-Morales, J. R.** (2016). Analysis
573 of cellular behavior and cytoskeletal dynamics reveal a constriction mechanism driving optic cup morphogenesis.
574 *Elife* **5**.
575 **Picker, A., Cavodeassi, F., Machate, A., Bernauer, S., Hans, S., Abe, G., Kawakami, K., Wilson, S. W. and Brand,**
576 **M.** (2009). Dynamic coupling of pattern formation and morphogenesis in the developing vertebrate retina. *PLoS*
577 *Biol* **7**, e1000214.
578 **Pottin, K., Hinaux, H. and Rétaux, S.** (2011). Restoring eye size in Astyanax mexicanus blind cavefish embryos
579 through modulation of the Shh and Fgf8 forebrain organising centres. *Development* **138**, 2467-76.
580 **Rembold, M., Loosli, F., Adams, R. J. and Wittbrodt, J.** (2006). Individual cell migration serves as the driving force
581 for optic vesicle evagination. *Science* **313**, 1130-4.
582 **Rétaux, S. and Casane, D.** (2013). Evolution of eye development in the darkness of caves: adaptation, drift, or
583 both? *Evodevo* **4**, 26.
584 **Rohr, K. B., Schulte-Merker, S. and Tautz, D.** (1999). Zebrafish zic1 expression in brain and somites is affected by
585 BMP and hedgehog signalling. *Mech Dev* **85**, 147-59.
586 **Sanek, N. A., Taylor, A. A., Nyholm, M. K. and Grinblat, Y.** (2009). Zebrafish zic2a patterns the forebrain through
587 modulation of Hedgehog-activated gene expression. *Development* **136**, 3791-800.
588 **Schindelin, J., Arganda-Carreras, I., Frise, E., Kaynig, V., Longair, M., Pietzsch, T., Preibisch, S., Rueden, C.,**
589 **Saalfeld, S., Schmid, B. et al.** (2012). Fiji: an open-source platform for biological-image analysis. *Nat Methods* **9**,
590 676-82.
591 **Sidhaye, J. and Norden, C.** (2017). Concerted action of neuroepithelial basal shrinkage and active epithelial
592 migration ensures efficient optic cup morphogenesis. *Elife* **6**.
593 **Simon, V., Hyacinthe, C. and Retaux, S.** (2019). Breeding behavior in the blind Mexican cavefish and its river-
594 dwelling conspecific. *PLoS One* **14**, e0212591.
595 **Stahl, B. A., Peuss, R., McDole, B., Kenzior, A., Jaggard, J. B., Gaudenz, K., Krishnan, J., McGaugh, S. E., Duboue,**
596 **E. R., Keene, A. C. et al.** (2019). Stable transgenesis in Astyanax mexicanus using the Tol2 transposase system.
597 *Dev Dyn*.
598 **Stemmer, M., Schuhmacher, L. N., Foulkes, N. S., Bertolucci, C. and Wittbrodt, J.** (2015). Cavefish eye loss in
599 response to an early block in retinal differentiation progression. *Development* **142**, 743-52.
600 **Stigloher, C., Ninkovic, J., Laplante, M., Geling, A., Tannhauser, B., Topp, S., Kikuta, H., Becker, T. S., Houart, C.**
601 **and Bally-Cuif, L.** (2006). Segregation of telencephalic and eye-field identities inside the zebrafish forebrain
602 territory is controlled by Rx3. *Development* **133**, 2925-35.
603 **Strickler, A. G., Famuditimi, K. and Jeffery, W. R.** (2002). Retinal homeobox genes and the role of cell
604 proliferation in cavefish eye degeneration. *Int J Dev Biol* **46**, 285-94.
605 **Strickler, A. G., Yamamoto, Y. and Jeffery, W. R.** (2001). Early and late changes in Pax6 expression accompany
606 eye degeneration during cavefish development. *Dev Genes Evol* **211**, 138-44.
607 **Take-uchi, M., Clarke, J. D. and Wilson, S. W.** (2003). Hedgehog signalling maintains the optic stalk-retinal
608 interface through the regulation of Vax gene activity. *Development* **130**, 955-68.
609 **Torres-Paz, J., Leclercq, J. and Retaux, S.** (2019). Maternally regulated gastrulation as a source of variation
610 contributing to cavefish forebrain evolution. *Elife* **8**.
611 **Torres-Paz, J. and Rétaux, S.** (2021). Pescoids and chimeras to probe early evo-devo in the fish Astyanax
612 mexicanus. *Frontiers in Cell and Devleopmental Biology* **in press**.
613 **Tropepe, V., Li, S., Dickinson, A., Gamse, J. T. and Sive, H. L.** (2006). Identification of a BMP inhibitor-responsive
614 promoter module required for expression of the early neural gene zic1. *Dev Biol* **289**, 517-29.
615 **Varga, Z. M., Wegner, J. and Westerfield, M.** (1999). Anterior movement of ventral diencephalic precursors
616 separates the primordial eye field in the neural plate and requires cyclops. *Development* **126**, 5533-46.
617 **Wilkens, H.** (2001). Convergent adaptations to cave life in the Rhamdia laticauda catfish group (Pimelodidae,
618 Teleostei). *Environmental Biology of Fishes* **62**, 251-261.
619 **Winkler, S., Loosli, F., Henrich, T., Wakamatsu, Y. and Wittbrodt, J.** (2000). The conditional medaka mutation
620 eyeless uncouples patterning and morphogenesis of the eye. *Development* **127**, 1911-9.

Wolff, C., Tinevez, J. Y., Pietzsch, T., Stamataki, E., Harich, B., Guignard, L., Preibisch, S., Shorte, S., Keller, P. J., Tomancak, P. et al. (2018). Multi-view light-sheet imaging and tracking with the MaMuT software reveals the cell lineage of a direct developing arthropod limb. *Elife* **7**.

Woo, K. and Fraser, S. E. (1995). Order and coherence in the fate map of the zebrafish nervous system. *Development* **121**, 2595-609.

Woo, K., Shih, J. and Fraser, S. E. (1995). Fate maps of the zebrafish embryo. *Curr Opin Genet Dev* **5**, 439-43.

Yamamoto, Y. and Jeffery, W. R. (2000). Central role for the lens in cave fish eye degeneration. *Science* **289**, 631-3.

Yamamoto, Y., Stock, D. W. and Jeffery, W. R. (2004). Hedgehog signalling controls eye degeneration in blind cavefish. *Nature* **431**, 844-7.

Young, R. M., Hawkins, T. A., Cavodeassi, F., Stickney, H. L., Schwarz, Q., Lawrence, L. M., Wierzbicki, C., Cheng, B. Y., Luo, J., Ambrosio, E. M. et al. (2019). Compensatory growth renders Tcf7l1a dispensable for eye formation despite its requirement in eye field specification. *Elife* **8**.

Main Figures and Legends

642

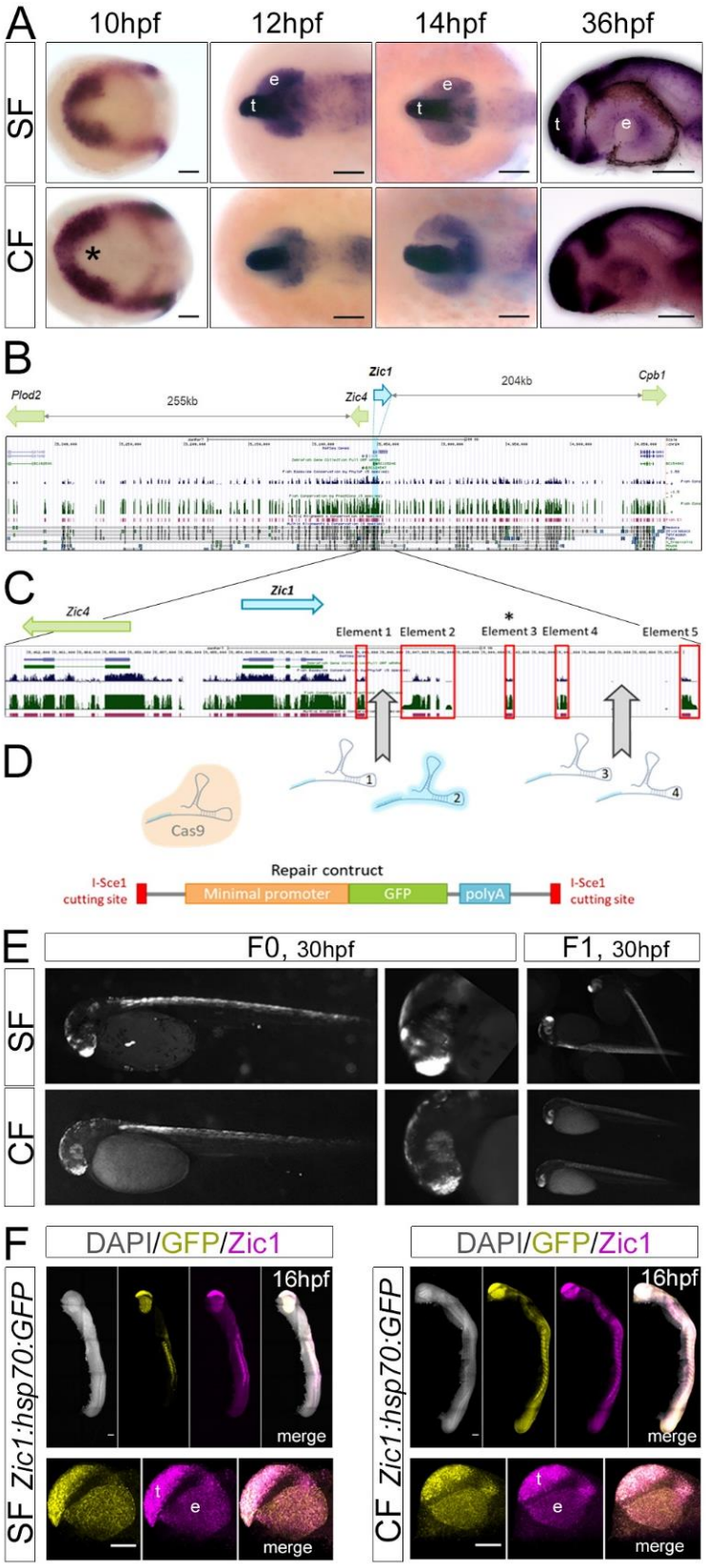

643

644 **Figure 1: establishment of surface fish and cavefish *Zic1:hsp70:GFP* lines.**

645 (A) *Zic1* expression at indicated stages in SF and CF. Anterior is to the left. Dorsal views at 10,
646 12 and 14hpf, lateral views at 36hpf. Asterisk: larger indentation in the CF eyefield.
647 (B) Zebrafish *Zic1* genomic region in UCSC genome browser (2010 assembly). Green blue peaks
648 as well as magenta and black elements correspond to high conservation, showing the
649 complexity of the region.
650 (C) Close-up on *Zic1*. Red boxes highlight conserved elements; element 3 is not conserved in
651 *Astyanax* (asterisk).
652 (C) sgRNA were designed to target the low-conservation regions between elements 1 and 2,
653 and 3 and 4. SgRNA2 (pale blue) efficiently generated cuts. It was co-injected together with
654 the Cas9 protein and the linear repair construct containing a minimal Hsp70 promoter and the
655 GFP.

656 (D) *Zic1-like* GFP fluorescence in mosaic F0s and stable F1s.

657 (E) Double-fluorescent *in situ* hybridization at 16hpf for *Zic1* (magenta) and *GFP* (yellow)
658 showing that the transgene recapitulates the endogenous *Zic1* pattern, both for SF and CF
659 lines. The top panels show entire embryos and the bottom panels show close-ups on the head,
660 including the *Zic1*-expressing telencephalon (t) and eye (e). Lateral views.

661 Scale bars=100µm.

662

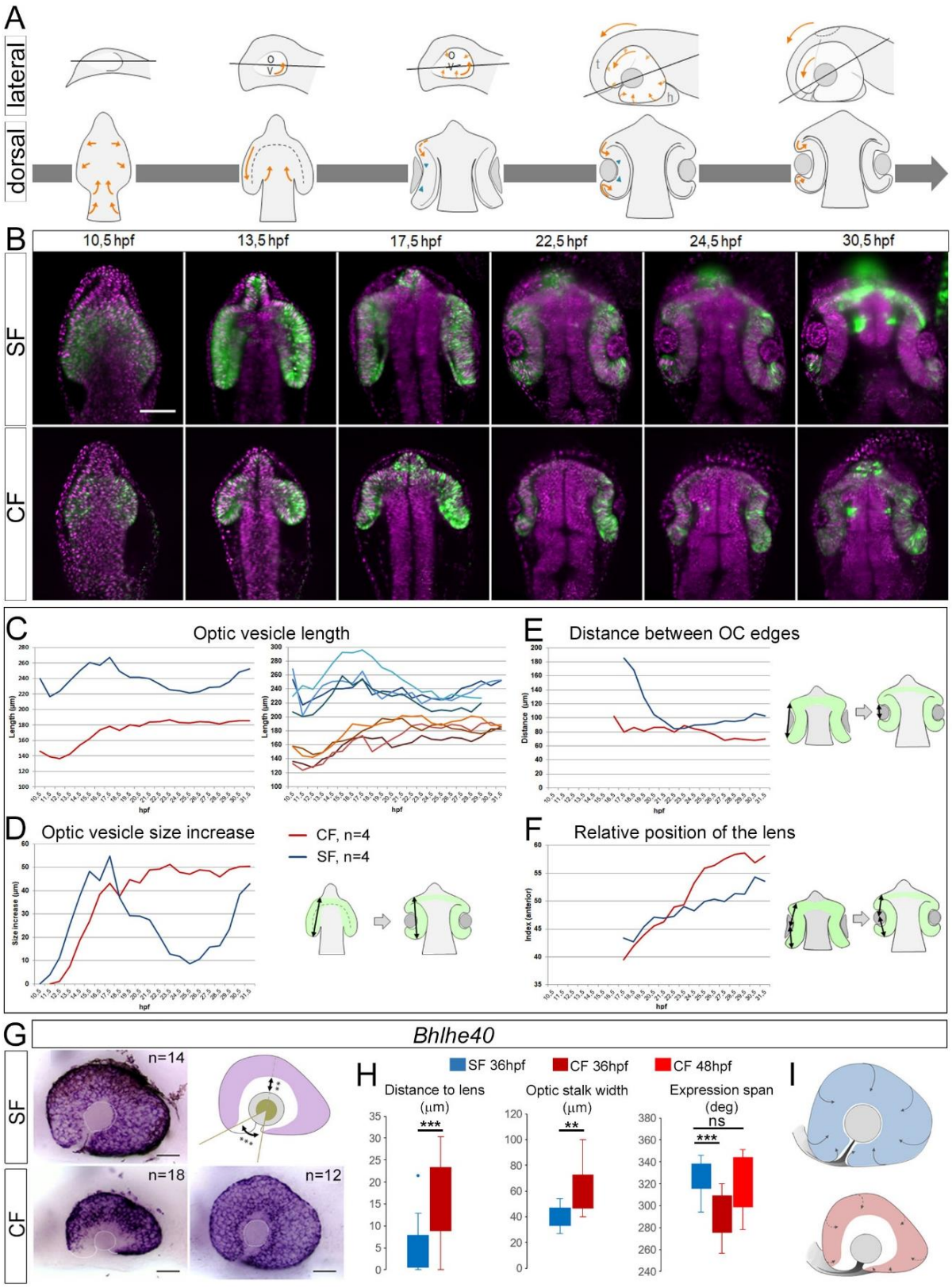

Figure 2: Live imaging and quantification of surface fish and cavefish eye morphogenesis.

666 (A) Schematic drawings of the main steps of eye morphogenesis in fish, in lateral (top) and
667 dorsal views (bottom). Orange arrows indicate cell and tissue movements; green arrowheads
668 show initiation of basal constriction. The grey line indicates the optical section plane used in
669 the pictures in B, which follows an optic stalk to lens center axis and accompanies the anterior
670 rotation illustrated by the arrows. All measures in C-F were done on these planes.
671 (B) Still images of time-lapse acquisitions from 10.5hpf to 30.5hpf on SF (top) and CF (bottom)
672 *Zic1:hsp70:GFP* lines (green, GFP; magenta, nuclear mCherry). Representative steps of eye
673 morphogenesis illustrating CF/SF differences are shown. Dorsal views, anterior to the top.
674 (C-F) Measurements. (C) OV length. The left graph shows the mean of n=4 eyes in each morph
675 (blue, SF; red, CF); the right graph displays the trajectories of individual eyes, showing the
676 reproducibility of the results. Measures are illustrated on the diagrams on the right. (D) OV
677 size increase. (E) Distance between the two optic cup edges. (F) Position of the lens relative to
678 anterior OV, showing that the lens is progressively shifted anteriorly between 25hpf and
679 30hpf.

680 (G-I) *Bhlhe40* expression. (G) In situ hybridization at 36hpf (left) and 48hpf (bottom right, CF).
681 The scheme shows the measures taken in (H). (I) Drawings illustrating comparative RPE
682 spreading in SF (top) and CF (bottom). Mann-Whitney test: ** $p<0.01$; *** $p<0.001$.
683

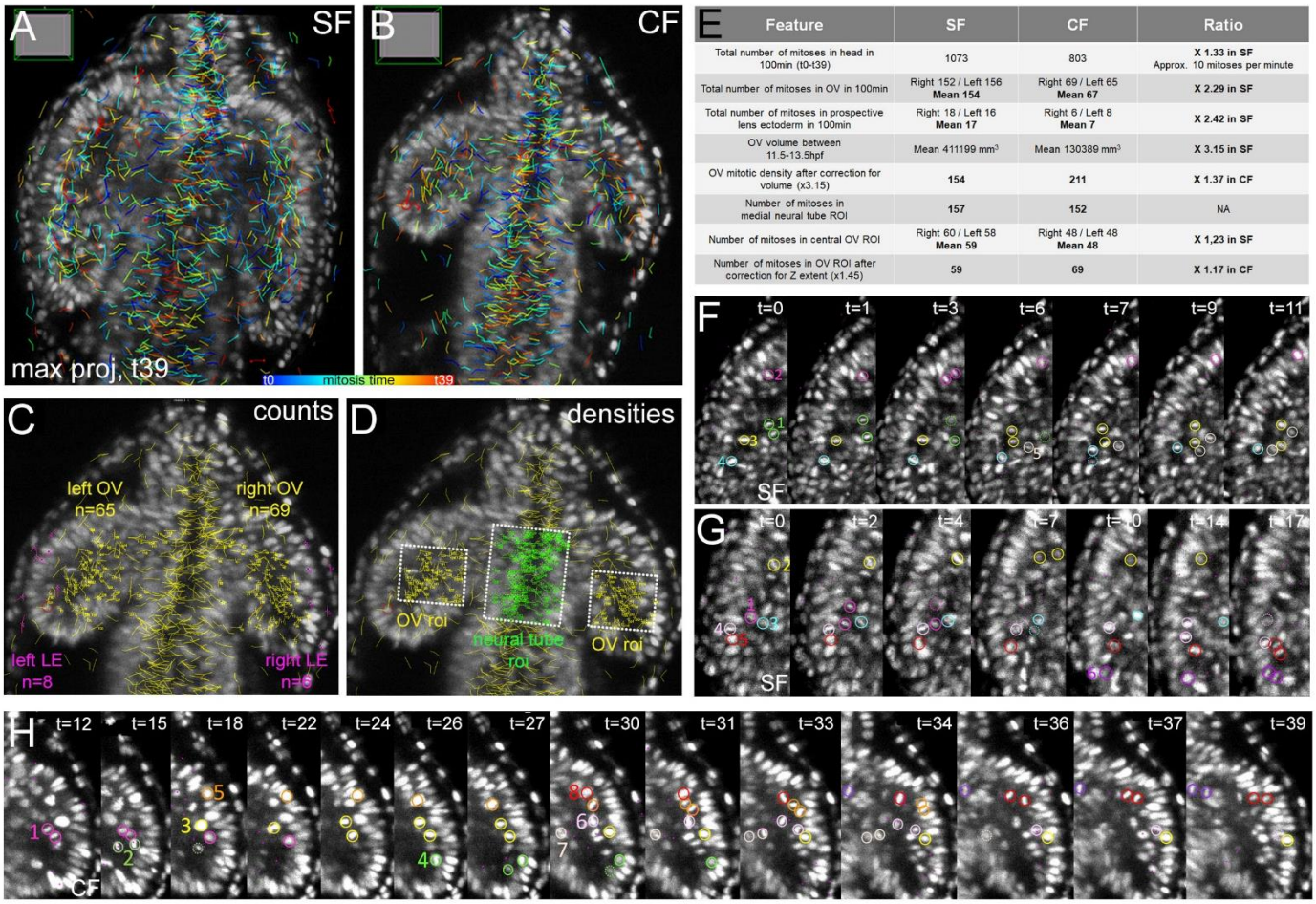

Feature	SF	CF	Ratio
Total number of mitoses in head in 100min (t0-t39)	1073	803	**X 1.33 in SF** Approx. 10 mitoses per minute
Total number of mitoses in OV in 100min	Right 152 / Left 156 **Mean 154**	Right 69 / Left 65 **Mean 67**	**X 2.29 in SF**
Total number of mitoses in prospective lens ectoderm in 100min	Right 18 / Left 16 **Mean 17**	Right 6 / Left 8 **Mean 7**	**X 2.42 in SF**
OV volume between 11.5-13.5hpf	Mean 411199 mm^3	Mean 130389 mm^3	**X 3.15 in SF**
OV mitotic density after correction for volume (x3.15)	**154**	**211**	**X 1.37 in CF**
Number of mitoses in medial neural tube ROI	**157**	**152**	NA
Number of mitoses in central OV ROI	Right 60 / Left 58 **Mean 59**	Right 48 / Left 48 **Mean 48**	**X 1,23 in SF**
Number of mitoses in OV ROI after correction for Z extent (x1.45)	**59**	**69**	**X 1.17 in CF**

Figure 3: Cell divisions.

(A,B) Mitotic embryos. All mitoses tracked during 100 minutes (40 time steps*2.5min) are shown on maximum projection dorsal views at t=39 (end of the movies) in SF (A) and CF (B). The color code indicates division time (see also **Fig. S5**).

(C) Mitosis counts, shown here on CF. After completion of tracking, each mitotic event was counted and re-allocated to regions of interest after manual re-segmentation (**Fig. S6**). Mitoses with yellow numbers belong to OVs, while mitoses with pink numbers belong to presumptive lens ectoderm.

(D) Mitosis densities were calculated to normalize for OV size differences in the two morphs, shown here on CF. The number of mitoses in a region of interest (roi) of identical size, either at the level of the OVs (yellow numbers) or the medial neural tube (green numbers), were counted in SF and CF (**Fig. S6**).

699 (E) Mitosis quantification and SF/CF comparison.

700 (F,G,H) Cell division behaviors. Colored circles help following individual cells. Representative
701 examples are shown in SF (F,G) and CF (H) OVs (time step: 2.5min). They were qualitatively
702 indistinguishable between SF and CF (more in **Fig. S6**).

703

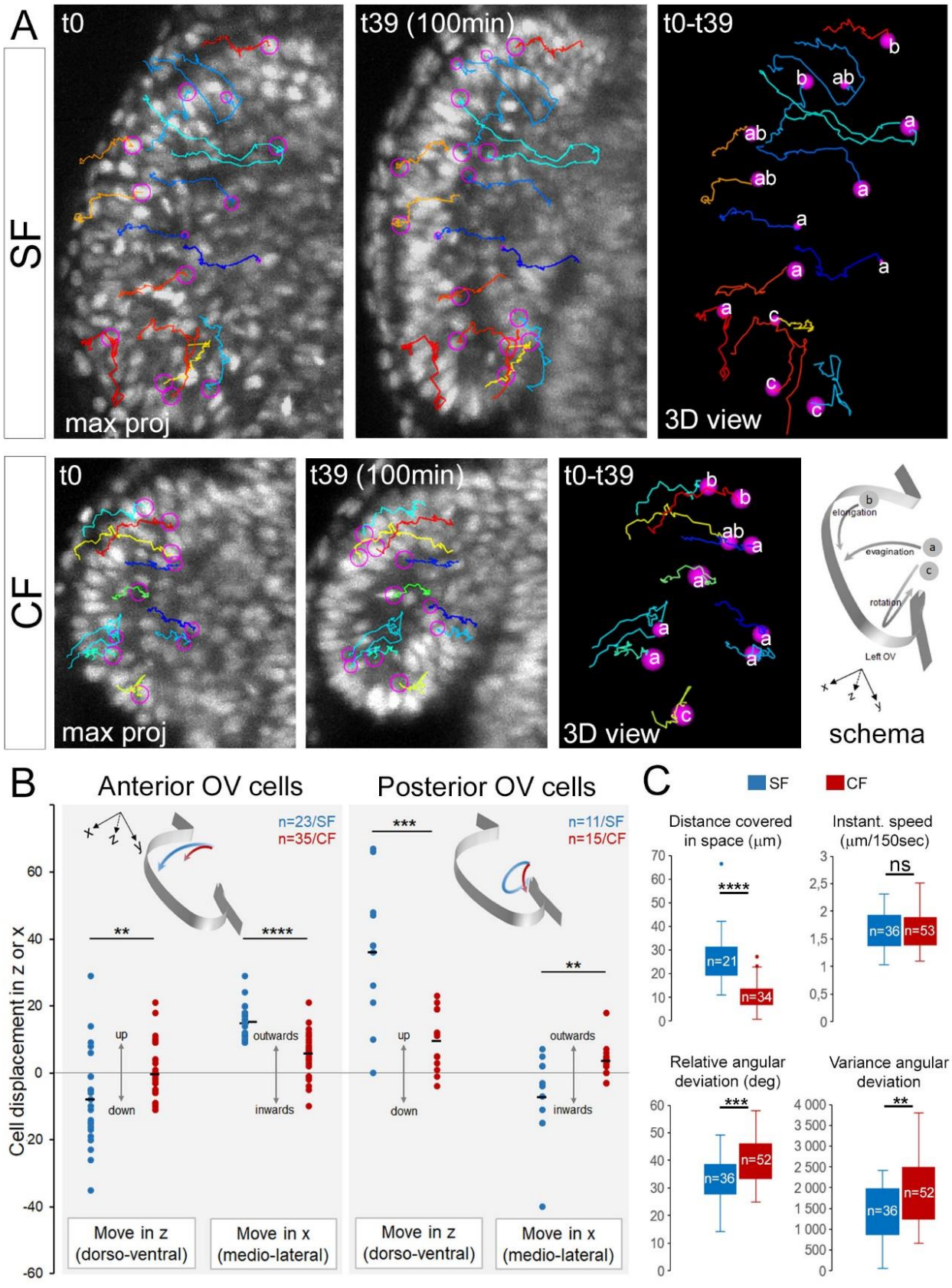

704

705 **Figure 4: Cell trajectories.**

706 (A) Cell tracking and trajectories. Representative examples of cells tracked during 100 minutes,
707 shown on maximum projection dorsal views at t=0 and t=39 (start/end of the movies) and on
708 3D views at t=0. Individual cell tracks are in different colors, in SF (top) and CF (bottom); cell
709 positions are in pink circles. The bottom right schema illustrates the 3 main types of
710 trajectories (a/evagination; b/elongation; c/rotation).

711 (B) Quantifications of trajectories and directions followed by cells of the 2/3 anterior *versus*
712 1/3 posterior OV, in SF (blue) and CF (red).

713 (C) Cell migration parameters in SF (blue) and CF (red).

714 Mann-Whitney tests: * $p<0.05$; ** $p<0.01$; *** $p<0.001$.

Supplemental Figures and Legends

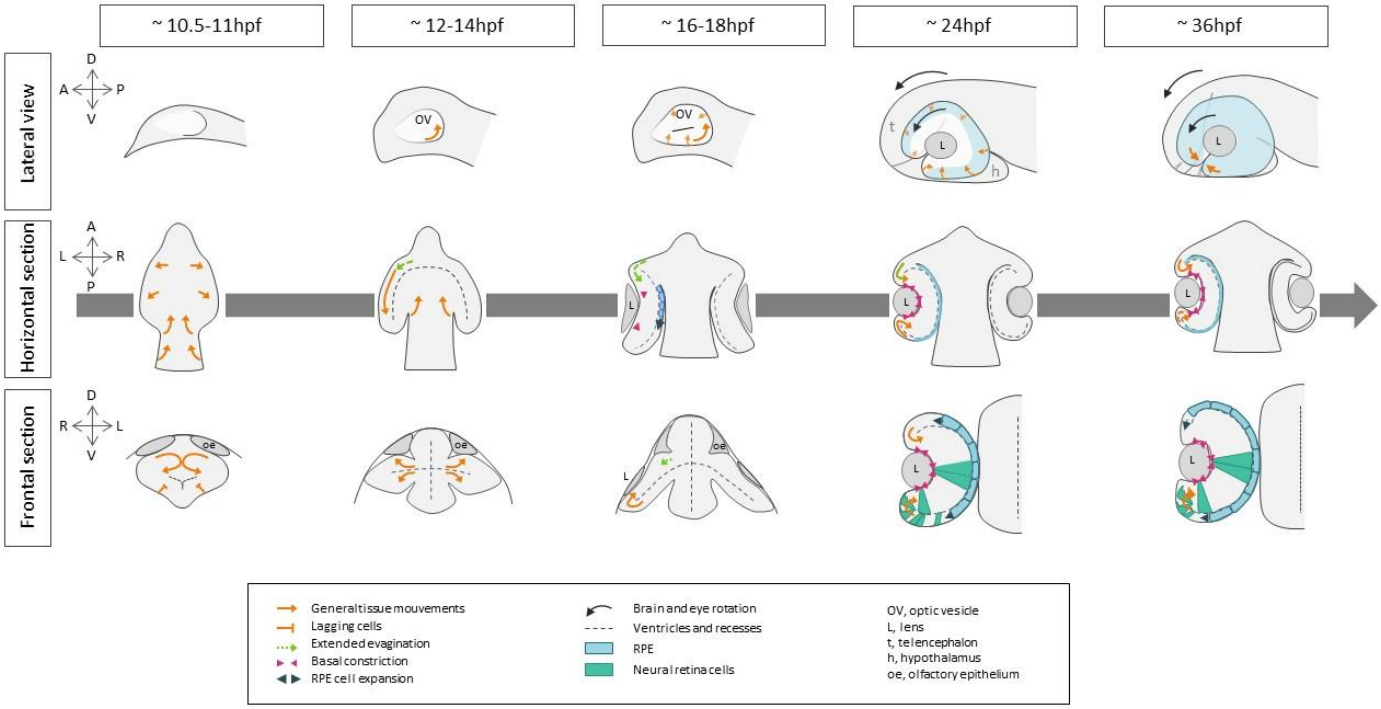

723

724 **Supplemental Figure 1: eye morphogenesis in fish.**

725 Schemes depicting the principal steps of eye morphogenesis in fish models, summarized
726 from the available literature cited in Introduction.

727 Stages and orientations are indicated.

728 Orange arrows show general cell and tissue movements.

729 Black arrows show the anterior-wise rotation of the eye and brain.

730 Green arrows show the contribution of extended evagination.

731 Pink arrowhead show cellular basal constriction.

732 The blue color depicts the RPE cells, while the green color depicts retina neuroepithelium cells
733 changing shape.

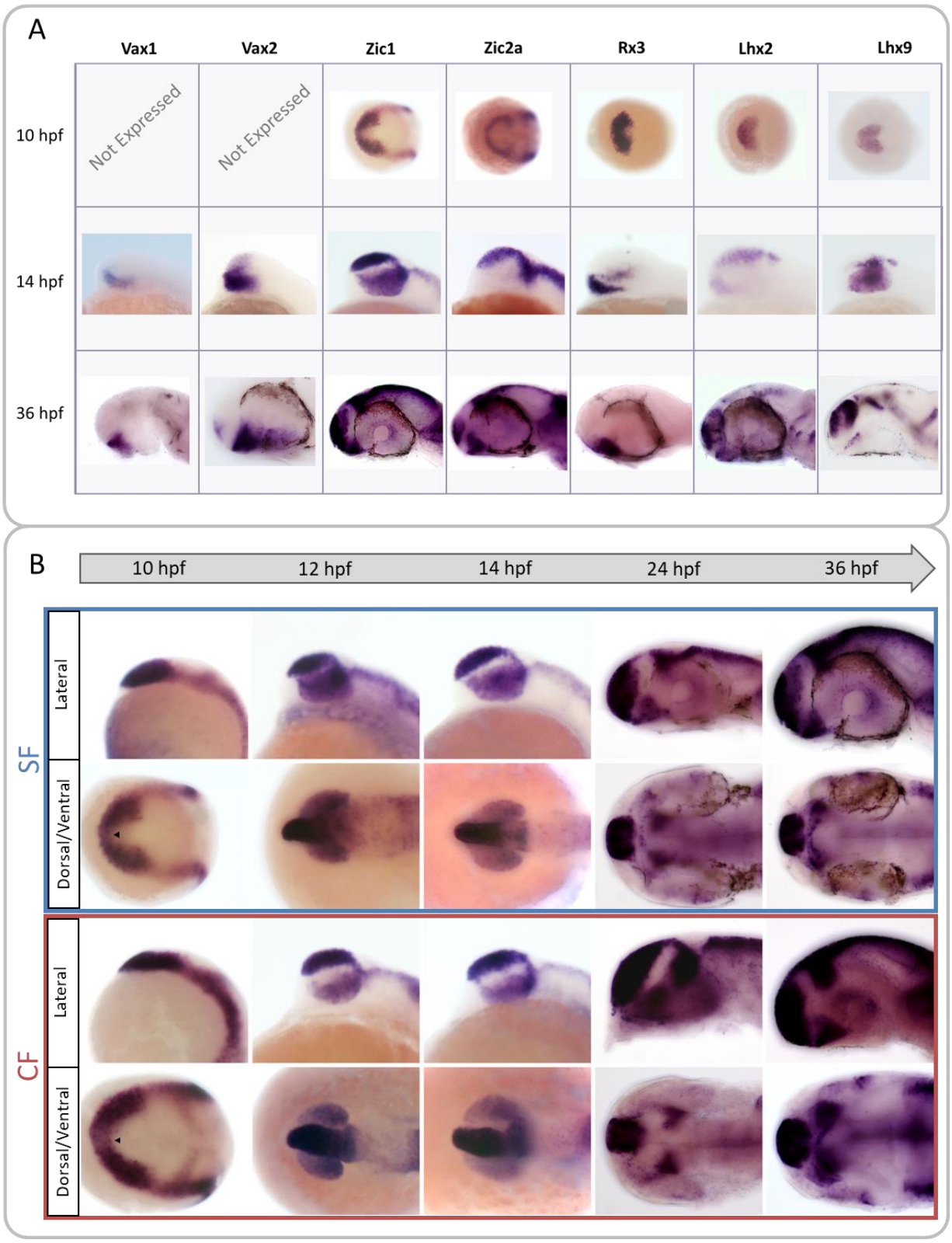

Supplemental Figure 2: choosing a candidate gene for transgenesis.

Chosen candidates were *Vax1*, *Vax2* (Take-uchi et al., 2003), *Zic1* (Hinaux et al., 2016; Maurus and Harris, 2009; Rohr et al., 1999; Tropepe et al., 2006), *Zic2a* (Sanek et al., 2009), *Rx3*

738 (Deschet et al., 1999; Rembold et al., 2006; Stigloher et al., 2006), *Lhx2* and *Lhx9* (Pottin et al.,
739 2011).

740 (A) Mini-screen of candidate genes by *in situ* hybridization at different stages (10, 12, 14, 24
741 and 36hpf) of interest on surface fish and cavefish (not shown) embryos. Anterior is to the left.
742 Dorsal views at 10hpf; lateral views at 14hpf and 36hpf. The eyes were dissected out for *Vax1*
743 and *Lhx9* (as no eye expression was detected for either of them) to allow better visibility of
744 the inner tissue. Among the 7 genes, 5 were expressed in the anterior neural plate at 10hpf
745 while 2 were not: *Vax1* and *Vax2*, whose expressions were detectable from 12hpf only. Five
746 of them were expressed at least partially in the OV per se (excluding ORR and optic stalk):
747 *Vax2*, *Zic1*, *Rx3*, *Lhx9* and *Zic2a* (faintly). At 36hpf, only 4 of them were still expressed in the
748 optic cup: *Zic2a* and *Zic1* (around the lens), *Lhx2* (faintly) and *Vax2* (in the ventral retina).
749 Subtle differences between CF and SF expression patterns were observed (not shown), and
750 only one candidate gene was consistently expressed in the eye from neural plate to 36hpf:
751 *Zic1.*
752 (B) Detailed analysis of *Zic1* expression pattern at 5 different stages in surface (SF) and cavefish
753 (CF). Anterior is to the left, at 10, 12 and 14hpf, bottom pictures are taken in dorsal view; at
754 24 and 36hpf, bottom picture are taken in ventral views. Arrowheads indicate an indentation
755 in the eyefield.

756 ***Description of expression patterns:***

757 *Vax1* expression was detectable from 12hpf in the presumptive ORR (between the OVs) and
758 additionally in the dorsal hypothalamus (according to brain axis (Puelles & Rubenstein, 2015),
759 closest to the ORR) and quite faintly in the ventral telencephalon.

760 *Vax2* expression was very similar to *Vax1* both in terms of onset of expression and pattern,
761 with the addition of the ventral quadrant of the eye. Although *Vax2* had a very interesting
762 ventral pattern, we discarded it as a candidate for transgenesis for its expression onset was
763 very late. Moreover, in *Vax2* enhancer trap zebrafish line (Kawakami Laboratory), the GFP
764 fluorescence is only visible at 18hpf (personal observation, data not shown).

765 *Rx3* expression showed a typical eyefield expression pattern at 10hpf but progressively faded
766 away during OV stages and was finally not expressed anymore at 24hpf. Conversely, an
767 anterior and ventral expression in the presumptive hypothalamus was detectable from 12hpf

768 and remained throughout the stages examined. At 36hpf, it was clear that only the dorsal half
769 of the hypothalamus, closest to the ORR, was labelled. Due to the rapid fading of its OV
770 expression, we did not consider *Rx3* as a valid candidate.

771 *Lhx2* and *Lhx9* were both already known to be expressed in the eyefield at neural plate stages
772 in *Astyanax* (Pottin et al., 2011). *Lhx2* expression showed very dim expression, if any, in the
773 OV at 12 and 14hpf but was expressed both in the prospective telencephalon and more faintly
774 in the prospective hypothalamus. Later on at 36hpf, *Lhx2* was expressed strongly in the
775 telencephalon and the olfactory epithelia; lighter expression was also visible in the ORR,
776 hypothalamus and sometimes eyes. Additional expression in the pineal, optic tectum and in
777 the hindbrain was also present.

778 *Lhx9* staining was strong in the OV at 12hpf (during evagination) and slightly lighter at 14hpf.
779 Moreover dorsal and ventral lateral labelling at the border of the neural keel and the OV
780 appeared, possibly prefiguring respectively the strong telencephalic staining visible at 24 and
781 36hpf and the hypothalamic cluster at the limit of the ORR already described in a previous
782 publication (Alié et al., 2018). At these late stages, we could not detect *Lhx9* expression in the
783 eye anymore. Salt and pepper staining was visible in the olfactory epithelia; a band of
784 expression outlining the optic tectum and lateral discrete marks in the hindbrain were present.
785 We did not choose *Lhx2* or *Lhx9* because of the rapid decay of their eye expression.

786 At 10hpf, *Zic2a* was expressed at the border of the neural plate and almost entirely
787 surrounding the eyefield except for a medial posterior gap. Faint staining in the bilateral
788 eyefield could also be seen on some embryos. At 12 and 14hpf, there was a strong *Zic2a*
789 expression in the telencephalon and a faint staining in the eye or distal part of the eye could
790 often be seen. Strong staining was generally visible throughout the dorsal-most brain. At
791 24hpf, *Zic2a* expression remained strong in the telencephalon and was also now strongly
792 visible at the border of the eye, in the ORR or optic stalk but without reaching the midline.
793 Faint staining in the eye remained. At 36hpf, the expression pattern was similar, with the
794 ORR/optic stalk staining reaching much closer to the midline. The eye expression was now
795 more focused around the lens, probably in the CMZ. Roof plate staining persisted throughout
796 development. Because *Zic2a* was never strongly expressed in the eye, we did not favour it as
797 a candidate for transgenesis.

798 *Zic1* was strongly expressed at 10hpf in the neural plate border and in the anterior neural
799 plate, at the level of the eyefield. At 12 and 14hpf, *Zic1* expression was consistently found in
800 the OV and between them (prospective ORR and optic stalk). A strong staining was also
801 present throughout the telencephalon. More posteriorly, the roof plate of the midbrain and
802 hindbrain was stained. The somites were also labelled. The pattern was very similar at 24hpf
803 and 36hpf with a strong telencephalic expression and a milder ORR expression (mainly
804 laterally and posterior to the optic recess)/optic stalk and eye staining (widely around the
805 lens). Roof plate and somites expression remained. Even though its pattern of expression was
806 complex and encompassed a region wider than the optic region of interest, *Zic1* was chosen
807 for transgenesis due to its early and persistent expression throughout the eye and the
808 ORR/optic stalk regions. Moreover, *Zic1* expression highlighted morphological differences
809 between SF and CF. At 10hpf, in CF *Zic1* was expressed in narrower lateral bands in the
810 eyefield, with a larger medial indentation. At 12hpf, *Zic1* pattern confirmed that the CF OV
811 were shorter and "plumper". At 36hpf the *Zic1*-expressing ORR was wider in cavefish.

812

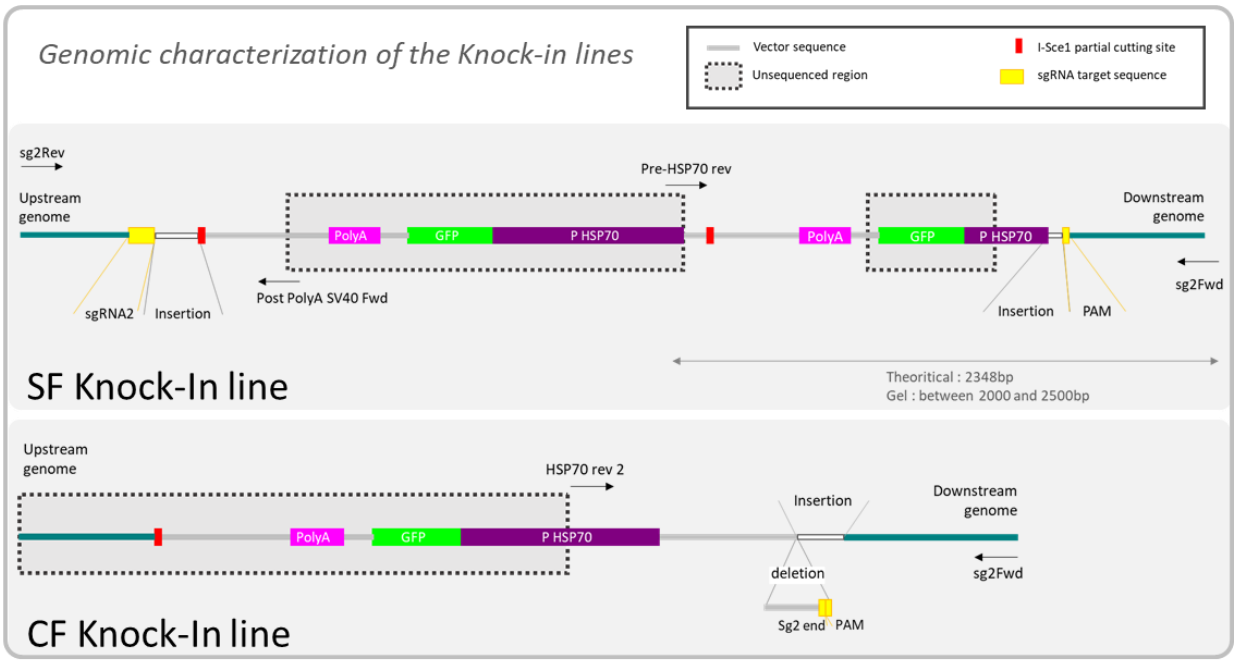

Supplemental Figure 3: genomic characterization of the Knock-in lines.

Knock-In insertions, based on partial sequencing. Dotted boxes indicate un-sequenced regions, leaving uncertainties. For example, in the surface fish line, there is at least a partial insertion of the repair construct, containing a truncated Hsp70 promoter and at least another insert in the same direction (but potentially several). Of note, the surrounding genomic region is very rich in T and A (GC content around 35%) with many repeats, making PCRs sometimes challenging.

The data show that for both lines the transgenes are inserted at the correct targeted site.

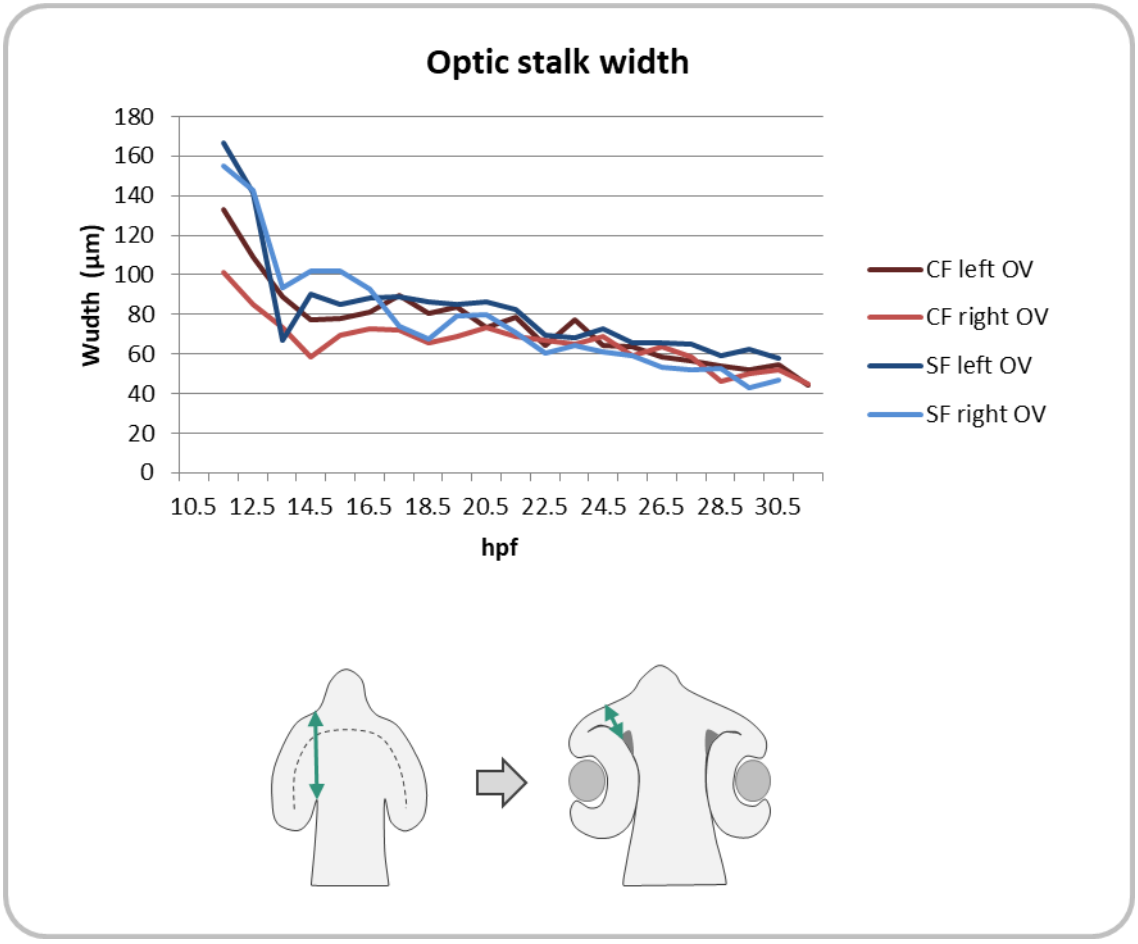

Supplemental Figure 4: optic stalk width.

The size of the optic stalk (in a wide meaning: the connection between the OV and the neural tube) is smaller in cavefish during early development due to the smaller size of the OV but rapidly becomes indistinguishable from the optic stalk of the surface fish.

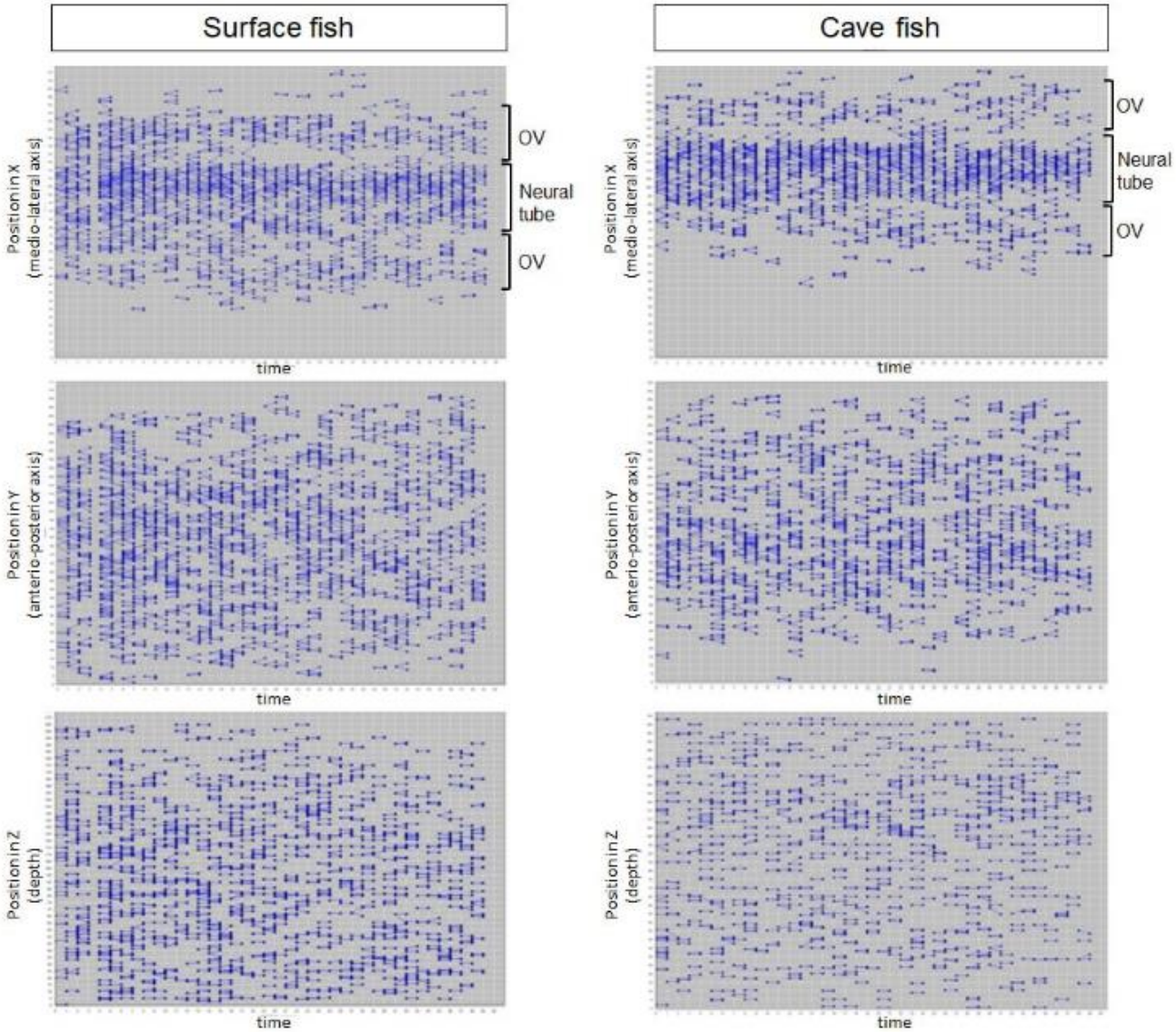

Supplemental Figure 5: Distribution of mitoses in the head and as a function of time, between 11.5hpf and 13hpf, in SF and CF embryos.

Plots showing the distribution of mitoses (schematically represented by a mother cell linked to daughter cells) in SF (left) and in CF (right). The 3 plots show the distribution of mitoses in X (medio-lateral axis), Y (antero-posterior axis) and Z (depth), as a function of time. Note the homogeneous repartition of divisions in the tissue, including in Z, suggesting that mitoses could be properly tracked, even in the depth of the tissue.

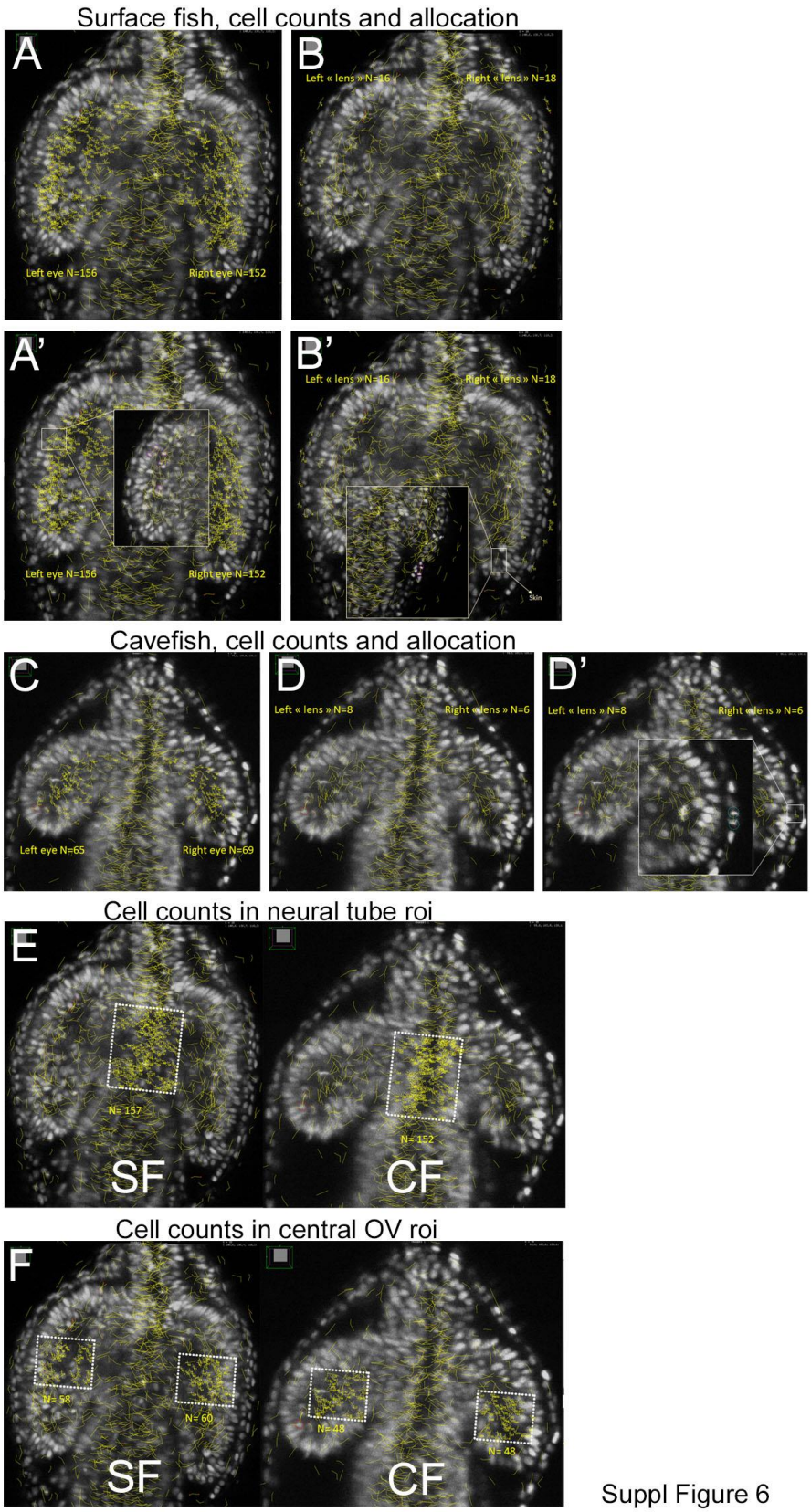

Suppl Figure 6

Supplemental Figure 6: Counting mitoses, and normalization.

845 (A-D') Illustration of the method used to count mitoses in SF (A-B') and CF (C-D'). To count
846 mitoses in OVs and presumptive lens without errors, each mitosis tracked and labelled in
847 MAMUT/Fiji was re-checked and segmented manually for proper allocation. Insets in A'B'D'
848 show examples of cells that appear like they belong to the OV region on the maximum
849 projection, but that were attributed either to the OV, the skin or the lens after manual re-
850 segmentation.
851 (E) Illustration of mitosis counts in a medial neural tube roi of the same size in SF and CF, for
852 estimation of mitotic density in the tissue.
853 (F) Illustration of cell counts in OV roi of the same size in SF and CF for estimation of mitotic
854 density in the tissue. Here, because the CF optic vesicles are smaller in XY but also in Z (depth),
855 a normalisation factor was applied. In SF, OV cell divisions were tracked along a Z extent of
856 145, while in CF cell divisions were tracked on a Z extent of 100. The normalisation factor was
857 therefore x1.45 (**Fig. 3E**).
858

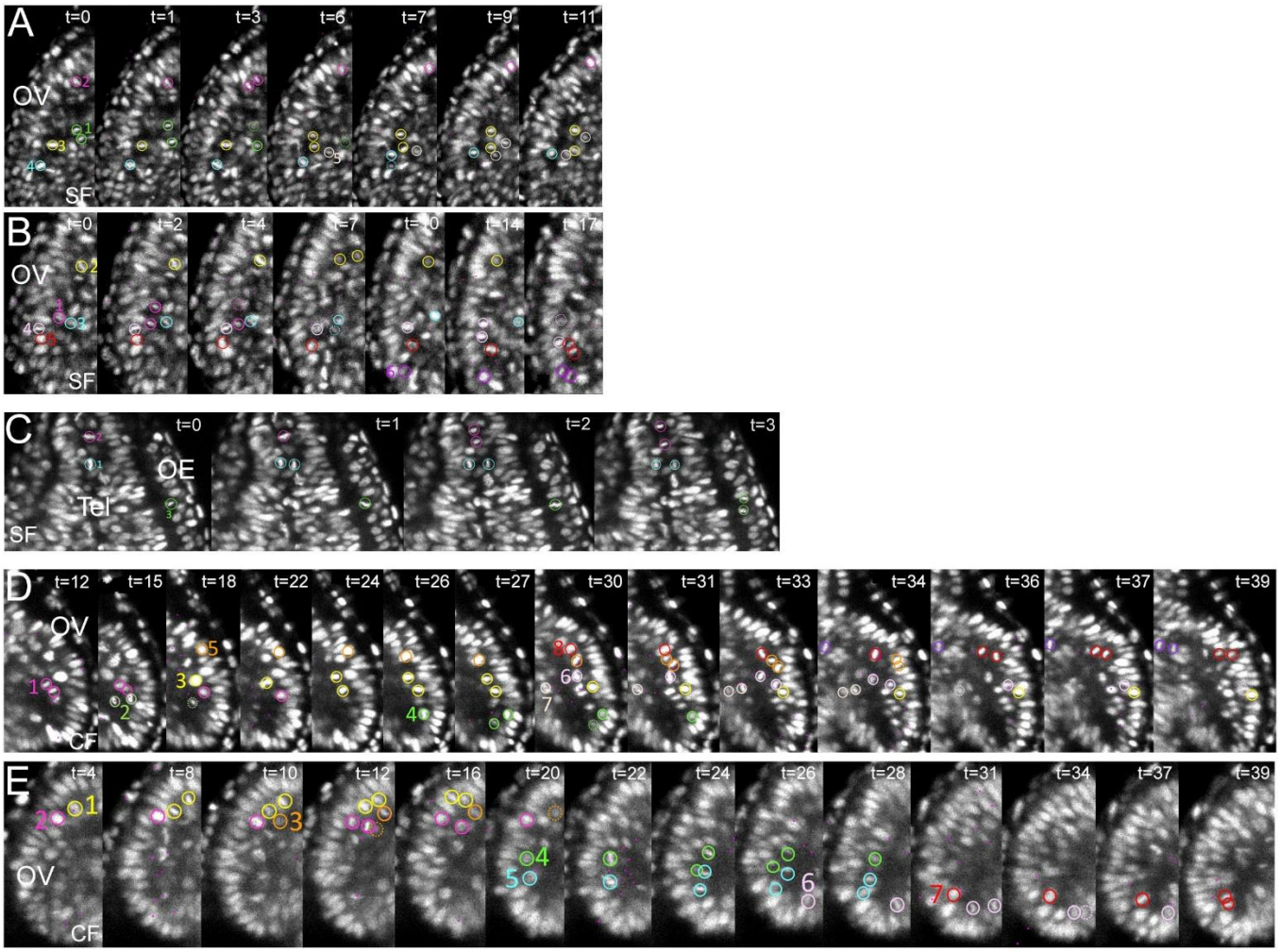

Supplemental Figure 7: Additional examples of mitotic behaviors at high power magnification, with comments.

Cell nuclei are labelled with colored circles; numbers indicate the order in which tracked cells will divide; daughter cells that migrate and that are lost in Z in the plane shown are indicated by dotted circles.

(A,B) show the same cell divisions sequence as in Figure 3, in the SF OVs.

<u>Comment for A:</u> The pink cell (#2) divides along the ventricle in the anterior OV and its daughter cell migrates and rapidly integrates in the neuroepithelium. The green and the beige cells (#1 and #5) divide in the proximal side of the ventricle and their daughter cells move towards the inner leaflet of the OV. So does the yellow cell (#3), although its initial position is

870 more distal. Note the rotation/orientation behavior of the metaphasic plate of the blue cell,
871 before dividing (#4).

872 (C) shows cell divisions in the telencephalon (Tel) and the olfactory epithelium (OE) of SF. The
873 pink and the blue cells (#1 and 2) divide in the telencephalon along the ventricular border,
874 with orthogonally-oriented metaphasic plates. The green cell (#3) divides in the olfactory
875 epithelium.

876 (D,E) show cell divisions sequences in the CF OVs. D is the same sequence as in Figure 3.

877 Comments for D: The pink (#1), yellow(#3), rose (#6) and red (#8) cells are representatives of
878 all those cells that divide at the ventricle and then rapidly migrate to incorporate in the
879 neuroepithelium. The orange cell (#5) follows a typical complete sequence: delamination from
880 neuroepithelium, division at the ventricle, and reintegration of daughter cells back in the
881 neuroepithelium. The kaki (#2) and the beige (#7) cells divide and populate the inner leaflet
882 of the OV. The purple cell divides at the level of the optic recess region (ORR).

883

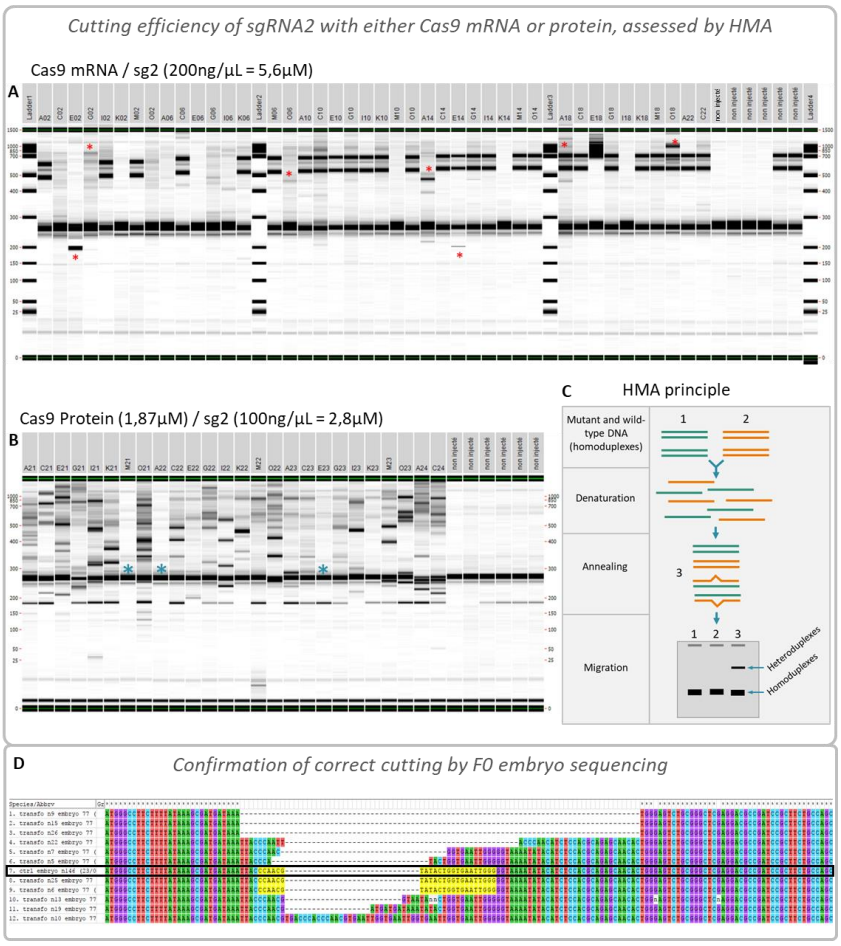

884

885

886 **Supplemental Figure 8: cutting efficiency of sgRNA 2**

887 (A) Assessment of sgRNA 2 cutting efficiency when injected with Cas9 mRNA by heteroduplex
888 mobility assay (HMA, explained in (C)). Each column is an individual F0 embryo. Embryos with
889 strong additional bands are labelled with a red asterisk; additional light bands can be seen in
890 several individuals, indicating cuts and imprecise repairs. Note that the 2 heavy bands seen on
891 many embryos are also present in some of the un-injected controls (the 6 columns on the
892 right) indicating a polymorphism in this region in the wild-type fish (not on the sgRNA target
893 sequence).

894 (B) Assessment of sgRNA 2 cutting efficiency when injected with Cas9 protein, note the strong
895 presence of additional band compared to the 6 control embryos on the right. Embryos without
896 any visible cuts are labelled with a blue asterisk. Additional bands are seen much more
897 frequently and are much more important than with the Cas9 mRNA injection, probably
898 indicating more frequent but also more precocious cut and repair events in the embryo, so
899 that many cells share the same sequence.

900 (C) Principle of the heteroduplex mobility assay: in an electrophoresis, heteroduplexes are
901 slowed down compared to homoduplexes so that they form additional bands that can be seen
902 even if the polymorphism is only a single substitution. In short, the DNA fragments are
903 denatured and renatured to form heteroduplexes. An electrophoresis is then performed (here
904 with a LabChip, PerkinElmer) to detect the presence of polymorphism.
905 (D) Different cutting and repair events in a single injected embryo. A PCR was performed on
906 one injected embryo (100ng/µL sgRNA2, Cas9mRNA) around the sgRNA2 target site and the
907 product was cloned into pGEM-T Esay (Promega) and transformed into One shot TOP10
908 competent bacteria (Thermo Fischer). Plasmidic preparations from individual colonies were
909 then sequenced. Various sequences were obtained, evidencing different cut and repair events
910 in one single embryo. sgRNA2 target sequence is highlighted in yellow whenever intact. This
911 F0 fish harbours both insertions and deletions around the cutting site of sgRNA2. A non-
912 injected control fish sequence is included, outlined in black.